THESIS FOR THE DEGREE OF LICENTIATE OF ENGINEERING

Hydrogen sorption properties of Pd-based nanoparticles – the role of alloying and internal structure

CARL ÅKE EMIL ANDERSSON

Department of Physics

CHALMERS UNIVERSITY OF TECHNOLOGY

Gothenburg, Sweden 2024

Hydrogen sorption properties of Pd-based nanoparticles – the role of alloying and internal structure

CARL ÅKE EMIL ANDERSSON

Department of Physics
Chalmers University of Technology
SE-412 96 Gothenburg
Sweden
Telephone + 46 (0)31-772 1000

Cover:
A multi-alloy nanoparticle of complex internal structure under hydrogenation.

Printed by Chalmers Digitaltryck
Gothenburg, Sweden 2024

"Everything is connected but nothing is working"

- *Asteroid City*

Abstract

Nanostructures and nanoparticles are the fundamental building blocks for many nanotechnologies such as microelectronics, optical metamaterials, quantum technologies, catalysis and different kinds of sensors. Current fabrication methodologies for nanostructures enable an outstanding degree of control over their physical properties, such as size, shape and composition. However, despite this high degree of precision, when studies of the physical and chemical properties of individual nanoparticles in an ensemble are performed, a striking variation in the response from *a priori* identical particles is often found. This variation reveals that there is more to these nominally identical systems than what is described by their size, shape and composition. To shed further light on what causes the individuality of such nanostructures, high precision measurements and huge sample sets are often needed to generate the required amount of statistically relevant data. In the thesis, I present two different projects that aid in this endeavor by enabling the study of multiple different nanoparticle systems on the same sample, eliminating experiment-to-experiment uncertainties. In the first study (**I**), we have developed a microshutter tool for the nanofabrication of plasmonic metal alloys with single nanoparticle composition control on a single sample. We showcase how this technique has been used to investigate 38 different alloys each in 3 different binary alloy systems for their application in plasmonics and state-of-the-art plasmonic hydrogen sensing. In the second study (**II**), we have to different degrees deformed Pd nanoparticles in a systematic way on a single sample to investigate how the induced defects and plastic deformation affect the hydrogen sorption of the individual nanoparticles. This revealed the intricate interplay between particle morphology, internal structure and substrate interaction that decide the hydrogen sorption properties of supported Pd nanoparticles.

Keywords: plasmonics, nanoparticles, multiplexing, nanofabrication, hydrogen, hydride, sensor, palladium, alloy, defect engineering.

List of Appended Papers

This thesis is based on the following appended papers:

Paper I: Andersson, C.; Serebrennikova, O.; Tiburski, C.; Alekseeva, S.; Fritzsche, J.; Langhammer, C. A Microshutter for the Nanofabrication of Plasmonic Metal Alloys with Single Nanoparticle Composition Control. *ACS nano* **2023**, *17* (16), 15978-15988.

Paper II: Andersson, C.; Zimmerman, J.; Fritzsche, J.; Rabkin, E., & Langhammer, C. The impact of systematic plastic deformation on the hydrogen sorption properties of single Pd nanoparticles. (In manuscript)

My Contribution to Appended Papers

Paper I: I did the TEM and SEM imaging as well as the TEM EDX characterization. I performed the hydrogenation kinetics measurements, wrote the paper together with Christopher Tiburski and Christoph Langhammer.

Paper II: I performed the dicing, mask development, metal deposition, mask-lift off and annealing steps of the sample fabrication as well as proposed the sample design. I performed all hydrogenation experiments, all corresponding data analyzation and all SEM imaging except Figure 1f-i as well as produced all corresponding figures to the manuscript. I have written the manuscript together with Christoph Langhammer.

Related Publications Not Included in The Thesis

Altenburger, B.; **Andersson, C**.; Levin, S.; Westerlund, F.; Fritzsche, J.; Langhammer, C. Label-Free Imaging of Catalytic H_2O_2 Decomposition on Single Colloidal Pt Nanoparticles Using Nanofluidic Scattering Microscopy. *ACS nano* **2023**, *17* (21), 21030-21043.

Darmadi, I.; Piella, J.; Stolas, A.; **Andersson, C.**; Tiburski, C.; Moth-Poulsen, K.; Langhammer, C. Plasma cleaning of cationic surfactants from Pd nanoparticle surfaces: implications for hydrogen sorption. *ACS Applied Nano Materials* **2023**, *6* (10), 8168-8177.

Contents

1 Introduction 3
2 Thermodynamics and Kinetics 7
3 Physical Metallurgy 11
3.1 Defects in Metals 11
3.1.1 Point Defects 12
3.1.2 Dislocations 14
3.2 Interfaces 16
3.3 Phases 20
3.4 Alloying 21
4 The Palladium-Hydrogen System 25
4.1 Gibbs Free Energy Affecting Interactions in the Pd-H System 28
4.1.1 Binding Energy of H in Pd 28
4.1.2 Strain at the Phase Boundary 29
4.1.3 Effective Attractive H-H Interactions 30
4.1.4 Electronic H-H Interactions 31
4.1.5 External Strains 31
4.2 The Pd-H Phase Diagram 32
4.2.1 The Pd-H Phase Diagram for a Nano-Sized System 36
4.3 Alloying 37
4.4 The Role of Defects 38
4.5 The Big Picture 42
5 Experimental Methods 43
5.1 Single Particle Plasmonic Microscopy 43
5.2 Microshutter Nanofabrication 50
5.3 Nanoindentation 56
6 Outlook and Conclusions 59
Acknowledgments 65
References 67

1 Introduction

The continual miniaturization of technological systems has been one of the cornerstones of technological advancement in the last century. This progress has been famously exemplified by Moore's "law", which is an observation that since the 60's, the number of transistors in an integrated circuit has doubled about every second year (Figure 1).[1]

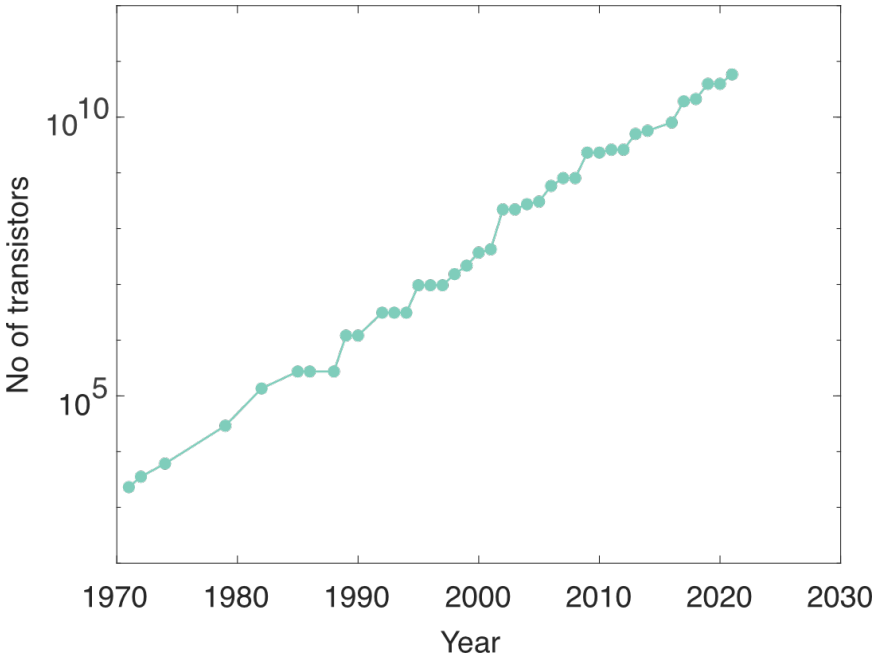

Figure 1: Typical number of transistors per commercial integrated circuit from 1970-2021.[2]

As technological systems have gotten smaller and smaller, also the tools to study and characterize the systems have become more advanced. Focusing on state-of-the-art transistors, their smallest features are nowadays on the order of a few atoms. At these sizes, structural imaging is non-trivial and today high-end electron microscopes are standard tools in nanofabrication

facilities around the world. In addition to electron microscopy, a whole array of different tools, *e.g.* atomic force microscopy (AFM), Raman spectroscopy, scanning-tunneling microscopy (STM) and X-ray diffraction (XRD) methods are available to researchers and industry to quantify the properties of nano-sized systems. Nonetheless, all these methods have in common that they either have a very high spatial resolution but low throughput – or vice versa. Therefore, methods that combine *both* aspects are in demand and continually developed, *e.g.* multi-beam scanning electron microscopes[3] and high-throughput synchrotron XRD beamlines.[4]

One area where it is especially critical with both high spatial resolution and high throughput is the field of nanoparticle science. Metallic nanoparticles have during the last 150 years been used with great success for heterogenous catalysis[5, 6], but in recent decades also for other applications such as nanosensors.[7] However, nanoparticles generated both by colloidal synthesis and of nanofabrication onto surfaces generally exhibit a great deal of individuality in their physical and chemical properties, extending even to particles on the same sample.[8-11] This means that not only are characterization methods needed that allow for single-particle measurements, but high throughput is also necessary to gather enough data for statistically relevant conclusions on why some particles behave different than others. In this thesis, three such methods – single particle plasmonic microscopy, microshutter nanofabrication, and nano-indentation – are applied to Pd-based nanoparticles in the context of their use for plasmonic hydrogen sensing.

In recent years, hydrogen has gained increased interest as a candidate of a carbon-free energy vector. This is apparent from large investments across the

Globe, for example the EU Hydrogen Strategy of the European Union[12], the U.S. National Clean Hydrogen Strategy and Roadmap[13] in the U.S.A., and national strategies in both Australia[14] and Japan[15]. However, if hydrogen is to achieve its full potential as a next-generation energy carrier, safe handling of the explosive gas is critical. To this end, the development of fast, reliable, and highly sensitive hydrogen detectors and sensors is of utmost importance. Nanoparticle-based sensors of different Pd alloys are some of the most promising systems for fulfilling the performance targets set by, for example, the U.S. Department of Energy[16]. However, there is still much to learn about these systems, *e.g.,* what are the optimal Pd-alloys and compositions for different sensing environments, and how do defects at the atomic level affect the hydrogen sorption properties of the nanoparticles?

In this thesis, I will shed light on some of these questions and more specifically, show how we can use single particle plasmonic microscopy, microshutter nanofabrication, and nano-indentation – to simultaneously screen many systems of different alloy composition and defect densities.

2 Thermodynamics and Kinetics

To describe the properties of a system in this thesis, *e.g.* hydrogen sorbing systems and metallic alloys, *thermodynamic* and *kinetics* considerations will be used. Due to their importance for my work, I will here spend a moment to define these two properties.

In this thesis, the thermodynamic considerations are used to describe the most energetically favorable state of a system under different steady-state conditions. This will generally be expressed in terms of Gibbs free energy[17]

$$G_{P,T} = U + PV - TS \tag{1}$$

which is a function that describes the energy of a system under constant pressure and temperature. In eq. (1), P is pressure, V is the volume of the system, T is the temperature and S is the entropy of the system. U is the internal energy of the system (*i.e.* the energy contained in the system at $P = 0\ ,\ T = 0$). The first two terms in eq. (1) are often combined into one entity[17]

$$H_P = U + PV \tag{2}$$

called the enthalpy of the system (also defined for constant pressure).
The concept of free energy is generally discussed as a direct comparison between the free energy of two different states of a system, *e.g.* two different

phases of a metallic alloy. Hence, we normally only consider the *difference* in free energy between two different states[17]

$$\Delta G = \Delta H - T\Delta S \tag{3}$$

rather than actually calculating the full Gibbs free energy G (hereafter referred to only as "free energy") for any of the states. The laws of thermodynamics state that a system wants to minimize its free energy, which in turn means that the most energetically favorable state of a system will be the state with the most (negative) ΔG compared to the other states.[17]

Even though the concept of free energy minimization tells us which state a system strives towards, it does not tell us anything about how fast this process will proceed. Here is where kinetics come into the picture. For example, free energy minimization can tell us that, at a certain partial hydrogen pressure, it's more beneficial for a hydrogen atom to reside inside the bulk of Pd on an interstitial site, rather than staying in the gas phase in its molecular state (more on this in chapter 4). However, to figure out how fast the hydrogen will reach the interstitial lattice position in the Pd bulk, we need to look at the kinetic properties of the process. In this thesis, the rate k of most processes will follow the Arrhenius equation[18]

$$k = Ae^{\frac{-E}{k_B T}}$$

(4)

where E is the energy barrier of the transition, T is the temperature, k_B is the Boltzmann constant and A is a process specific constant (the "pre-exponential factor"). In the case described earlier with a hydrogen atom diffusing into Pd bulk, we have multiple transition steps – H_2 dissociating into 2 H on the Pd surface, H moving from surface to subsurface and from subsurface to bulk etc. (more on this in chapter 4) – each with their own energy barrier and, hence, different rates according to eq. (4). In experiments, we can not generally distinguish between the elementary different steps of a process, which means that we need to modify eq. (4) by replacing E for every step with the apparent energy E_a of the entire process. This apparent energy can be viewed as a weighted average of the enthalpy difference between all the different states (intermediates, transition states, products etc.) of the reaction.[19]

3 Physical Metallurgy

In this chapter, I will review some concepts of classic physical metallurgy. Physical metallurgy deals with relating the microstructure of metals and alloys to their physical properties. That I here also add the word “classic” is to emphasize that the concepts discussed in this chapter holds for describing the properties of *macroscopic* metals and may therefore not always apply to the nano-sized systems mainly discussed in this thesis. With this said, the concepts discussed in this chapter should serve as a good foundation for gaining an understanding of how the internal structure of metallic nanoparticles might affect their individual physical and chemical properties. Specifically, the first section of this chapter delves into the different types of defects we can find in metals and how these affect the strength and diffusion properties inside the metal. In the second section, I will briefly discuss what we mean with different phases of metals and explain two different types of phase transitions that will be important further on when we look at the Pd-H system in chapter 4. Finally, in the last section I will introduce the concept of alloying and how this can be used for understanding traditional metallic alloys and how many of the concepts carries over to the Pd-H system.

3.1 Defects in Metals

The atoms of metals are arranged in a periodic structure called a crystal lattice.[20] Many of the physical properties of metals (and also other crystalline materials) can be directly traced back to this ordered and repeating structure. Even if the (infinitely) ordered array of atoms is the main characteristic of a theoretically “perfect” crystal, real crystals often contains different types of imperfections. These imperfections have profound effects on the physical

and chemical characteristics of the material, such as mechanical strength and solute diffusivity. In fact, many metallic materials – such as different versions of steel – are engineered to *have* defects, as these give the desired properties of the material. The different defects that we will look closer at in the following sections are i) point defects, ii) edge and screw dislocations and iii) grain boundaries.

3.1.1 Point Defects

Point defects are imperfections resulting from either the addition or removal of a single atom from/into the crystal lattice. The two most important point defects are interstitials and vacancies.

An *interstitial* is an addition of an extra atom into the lattice. If all the lattice sites around the extra atom are occupied, the extra atom occupies a position in between its neighbors, displacing them slightly from their equilibrium positions in the process. This is depicted in Figure 2a. In most contexts involving interstitials the added atom is not of the same element as the rest of the lattice. The removal of an atom from the lattice is called a *vacancy* and is depicted in Figure 2b. This defect instead leaves a gap in the lattice.

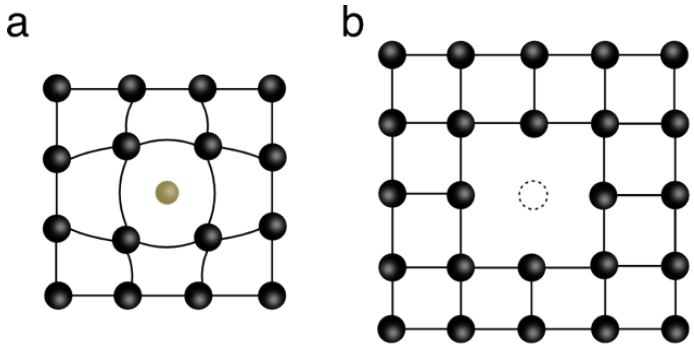

Figure 2: Schematic of point defects in a crystal lattice. (a) Interstitial and (b) vacancy.

Interstitials induce strain in their neighboring region and as a result increase the free energy of the system.[21] In the case of vacancies however, the change in entropy caused by the vacancy is generally enough to overcome the enthalpy of formation for the vacancy, and as such the free energy of the system is decreased.[22] This means that for elevated temperatures, having a certain concentration of vacancies actually is energetically favorable for the system.[21, 22] This concentration of vacancies in the solid, X_v, is expected to follow the relation[21, 22]

$$\mathrm{X_v} = exp\frac{\mathrm{\Delta S_{vib}}}{\mathrm{k}}\exp\left(-\frac{\mathrm{\Delta E_v}}{\mathrm{kT}}\right) \tag{5}$$

where ΔS_{vib} is the change of vibrational entropy per vacancy, ΔE_v is the vacancy energy of formation, k is the Boltzmann constant and T is the temperature.[21] From equation (5), it is clear that we in any system with $T > 0$ can expect a certain number of vacancies and also that the number of vacancies will increase with increased temperature.

The most important feature of vacancies in the context of this thesis is that they aid the diffusion of atoms through the lattice. This is due to the vacancy substantially lowering the energy for atoms to change position within the lattice, and as such, increase diffusivity.[21]

3.1.2 Dislocations

Dislocations are a type of defect that consists of entire rows of atoms being displaced or arranged anomalously. As such, they are called *linear* or *line* defects. The two simplest types of dislocations are *edge* and *screw* dislocations, and one can create all other types of (linear) dislocations by linear combinations of these two types of dislocations.[21]

An edge dislocation is essentially an extra half crystal plane inserted into the lattice. In other words, imagine that over a distance x along a row of atoms in a crystal plane we have 6 atoms (Figure 3a). For all rows of atoms beneath this initial row we also have 6 atoms along the same distance. However, in the row above the initial row, and for all further rows above, we instead have 7 atoms along the same distance x. This is the essence of an edge dislocation and is depicted in Figure 3a.

For a screw dislocation, one can imagine that a cut has been made partly through the lattice and that the crystal on both sides of this imaginary cut has been twisted with respect to each other. This creates a twisted distortion of the lattice, as depicted in Figure 3b.

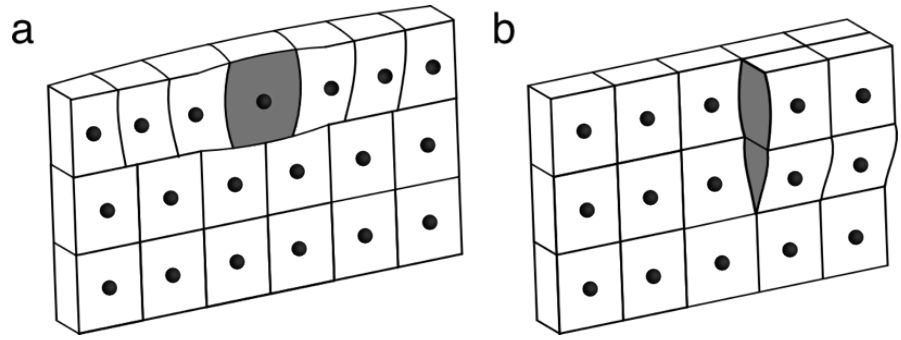

Figure 3: Dislocation in a crystal lattice. (a) Edge and (b) screw dislocation. The origins of the lattice misfits, the extra atoms in (a) and the lattice distortion in (b) are highlighted in gray.

Both types of dislocations, edge and screw, increase the free energy of the system, but contrary to vacancies, they are not thermodynamically favored at any temperature.[21] For all temperatures, they increase the free energy of the system. Their appearance is instead normally a fabrication consequence. If the technique used to make the material is unable to provide the environment necessary for a perfect crystal to form, dislocations have a high probability of forming. Even for fabrication techniques routinely used to make single crystals (that is, crystals only consisting of a single grain), such as colloidal synthesis of nanoparticles, may still introduce dislocations in the resulting crystal structure.[23, 24] In the case of nanoparticles, one of the ways to create (nearly) dislocation free crystals is through solid-state-dewetting, a method that through the use of high temperature annealing and single crystal substrates provide the environment to form (nearly) defect-free nanoparticles.[25-29]

Having established the dislocation concept as such, it is interesting to discuss what effect dislocations have on the properties of metals. In a crystal, free of

dislocations and point defects, plastic deformation in response to an applied force, must be initiated through slip of an entire crystal plane.[21] The glide of the two planes in different directions, and the resulting plastic deformation, can then proceed. It is well known that the strength of metals (*i.e.* the amount of shear stress that the metal can withstand before plastic deformation) is well below the theoretical strengths expected from perfect crystals.[21, 27] Based on the work of G.I. Taylor[30], E. Orowan[31] and M. Polanyi[32] from 1934 it has then been established that glide of dislocations are the main contributor to the low strength of real metals compared to perfect crystals.

Also, just as with vacancies, dislocations are expected to aid diffusion of atoms through the crystal lattice.[21] This is called *pipe diffusion* and is generally attributed to the disordered dislocation region locally lowering the activation energy for diffusion through its path.[33, 34]

3.2 Interfaces

An *interface* in a crystal can be defined as a two (or three) dimensional region with broken atomic bonds for the atoms inside the region of interest.[21] This is a very broad definition, and we will soon see that we can divide interfaces into many subcategories. The many uncoordinated atoms of the interface locally increase the free energy of the system, but can lower the *overall* free energy of the system as they serve as termination points for stress fields that may have built up inside the crystal[21], *e.g.* external stresses like substrate clamping affecting a supported nanoparticle or stresses caused by mechanical work performed during traditional casting and blacksmithing.

Depending on how and where the interface has formed, we can define the following subcategories:

- The surface of the crystal. This is where the crystal lattice is terminated and is in contact with its environment. Surface atoms always have higher free energies than bulk atoms due to the many undercoordinated surface atoms.
- Grain boundaries. Here defined as the interface regions between crystallites in a solid that have different lattice orientations.[21]
- Incoherent phase boundaries. This type of interface we will examine in more detail in section 3.3.

We will from now on focus specifically on the grain boundary type interfaces. As grain boundaries are defined by crystallites with different orientation, one way to define them is by the direction of the rotation axis of the misorientation compared to the face of one of the crystallites in the grain boundary. If the rotation axis of the misorientation is parallel to the grain boundary face, we have a *tilt boundary* (see Figure 4a). If the rotation axis of the misorientation instead is perpendicular to the grain boundary, we have a *twist boundary* (see Figure 4b).

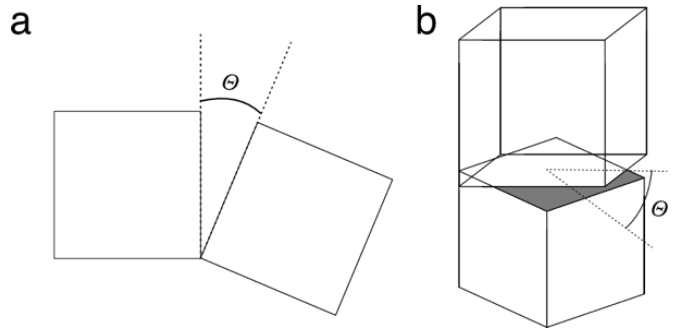

Figure 4: Schematic representation of two types of grain boundaries. (a) Tilt boundary and (b) twist boundary with θ as the misorientation angle.

We can further classify the two types of grain boundaries through the magnitude of the misorientation angle θ between the two different grains (Figure 5). If $\theta > 15°$, the boundary is called a *high-angle* grain boundary (Figure 5a) and if $\theta < 15°$, it is called a *low-angle* grain boundary (Figure 5b). The high-angle grain boundaries are generally associated with more open space between the grains and a higher interfacial energy from the surface of the grains compared to their low-angle counterparts.[21, 35] A twin-boundary (Figure 5d) is a special type of boundary, where the arrangement of atoms in the respective grains are mirrored along the boundary.

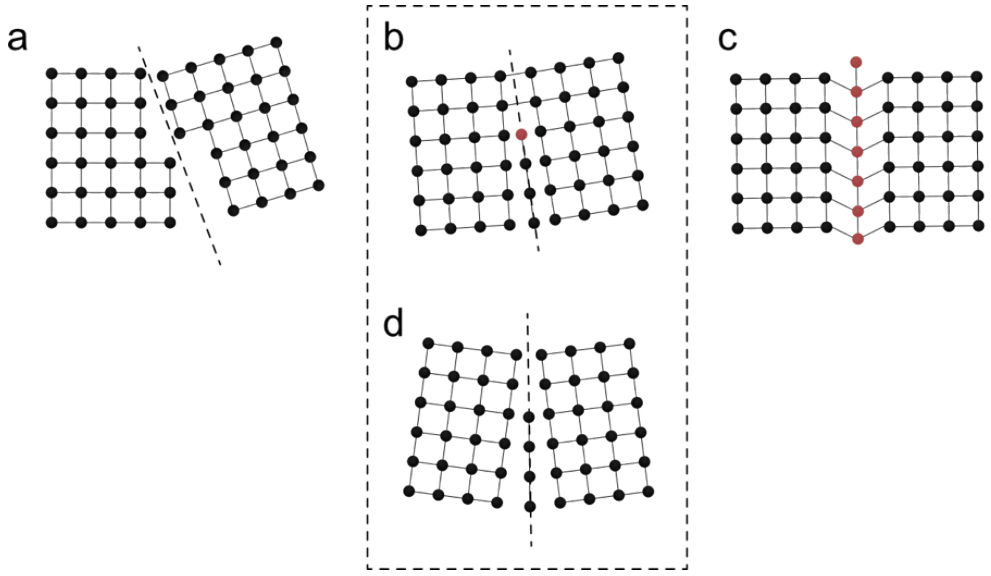

Figure 5: Different types of planar defects. (a) High-angle grain boundary (dashed line). The misorientation angle between the two grains of the boundary is $> 15°$. (b) Low-angle grain boundary (dashed line). The misorientation angle between the two grains of the boundary is $< 15°$. Low-angle grain boundaries can often be described as an array of dislocations (one dislocation highlighted as a red atom). (c) Stacking fault. A stacking fault is a special type of planar defect where the lattice points of an entire plane of atoms (red) is displaced compared to planes on either side. (d) Twin-boundary. A twin-boundary is a special type of boundary, where the arrangement of atoms in the respective grains are mirrored along the boundary (dashed line). Image adapted from Lu *et al.*[35]

Finally, as with vacancies and dislocations, grain boundaries are also expected to aid diffusion of atoms through the lattice.[21] Just as with dislocations, the increased diffusion is generally attributed to the disordered dislocation region locally lowering the activation energy for diffusion through the grain boundary.[33, 36] However, it should here be emphasized that due to the high degree of individuality of different grain boundaries and dislocation networks, it is very difficult to provide a generalized mechanism

that explain the kinetic accelerating for all different types of grain boundaries and dislocation networks.[37]

3.3 Phases

A very broad definition of a *phase* refers to different forms of the same material that have different physical properties but that are chemically uniform. A relevant example for this thesis is the two phases, α and β, of the palladium-hydrogen system. We will learn more about these two phases in chapter 4, but for now we will settle with stating that both phases consist of hydrogen atoms absorbed into the Pd metal lattice where they occupy interstitial lattice sites, but while the former has a lattice parameter of 3.895 Å, the latter instead has an expanded lattice parameter of 4.025 Å.[38]

The boundary between two phases in a crystal can either be *coherent* or *incoherent*. To describe the difference between the two, we will consider two hypothetical phases, α and β, of an imaginary metal *A*. The α-phase we assume has a lattice parameter of 2 Å and the β-phase a lattice parameter of 4 Å (*e.g.* due to inclusion of hydrogen interstitials as in a hydride). For a coherent phase boundary, the transition from a lattice parameter of 2 Å to 4 Å is continuous (Figure 6a). This leads to increased strain in the phase boundary, increasing the free energy of the system.[21] For an incoherent phase boundary, the atomic bonds between the two phases are broken, *e.g.* by means of dislocations or grain boundaries (Figure 6b). This leads to decreased strain compared to the coherent boundary, but instead increased interfacial energy due to the broken bonds.[21] As such, both types of phase boundaries increase the free energy of the system, such that which is the most energetically favorable one depends on the specific system.

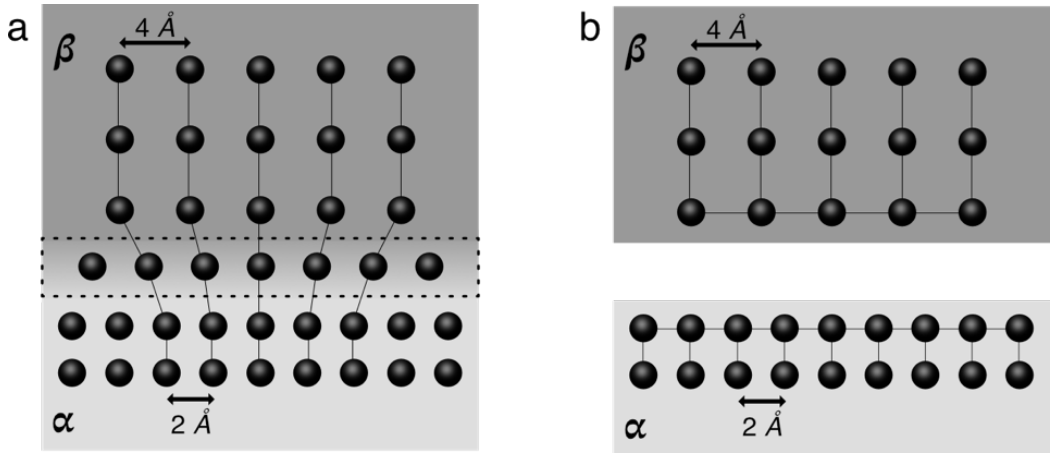

Figure 6: Schematic representing the two different types of phase boundaries between two imaginary phases α and β. (a) For a coherent phase boundary (dashed box), we have continuity between the crystal planes. This in turn introduces strain in the boundary. (b) For an incoherent phase boundary, the atomic bonds are in some way broken between the two phases, for example by means of dislocations or grain boundaries. This leads to decreased strain, but higher interfacial energy compared to (a).[21]

3.4 Alloying

Since the bronze age, alloying has been a cornerstone of metallurgy to improve and expand the physical and chemical properties of elemental metals. Taking bronze as an example, it is both harder and more durable than its constituents tin and copper, while at the same time melting at lower temperature than pure copper and hence being easier to cast into tools.[39] In this thesis, the main uses of alloying will be in regards to alloys of Pd and how this affects the hydrogen sorption properties of the alloys compared to

pure Pd. This will be further discussed in section 4.3. Here, I will give a more general introduction to the thermodynamics of alloying.

A critical tool when describing alloys are the so-called *phase diagrams*. Phase diagrams are, in essence, maps showing the most thermodynamically stable state (*i.e.* the state of lowest free energy G) of alloys under thermodynamic equilibrium as a function of different thermodynamical variables, most commonly temperature and composition for metallic alloys. To describe this in more detail, I will discuss a hypothetical binary alloy between the elemental constituents *A* and *B*.

First however, I will introduce two different types of atomic orderings that are important for metallic alloys. The first is the homogenous atomic ordering where atoms of the constituent elements are randomly dispersed among each other (Figure 7a). This is generally how atoms are dispersed in a liquid, and as such, this atomic ordering is often called *solid solution* when it occurs in the solid state. The other type of atomic ordering is a heterogenous atomic ordering. Here, some kind of long-range order exists that differentiates between two different phases of the alloy, either in terms of composition (Figure 7b) or some other physical property, *e.g.* lattice parameter, as will be the case when discussing the two phases of palladium hydride in chapter 4.

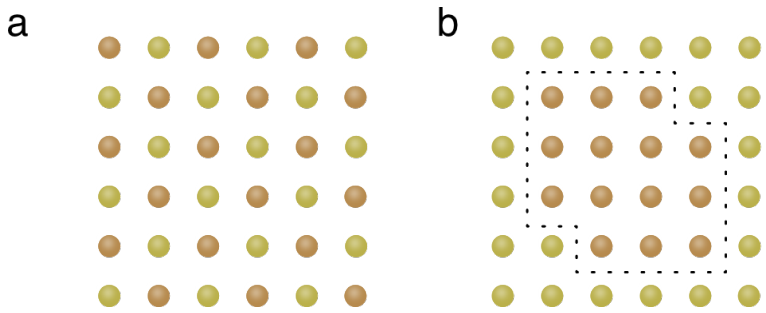

Figure 7: Two different types of atomic ordering in metallic alloys, here represented with a binary alloy of two constituent elements. (a) Homogenous ordering, also generally called "solid solution", in which the atoms of the two elements are randomly dispersed within each other. (b) Compositional heterogenous ordering. Here the atoms of the different element have clustered together in separate phases of distinct local compositions (outlined with a dashed line). In general, the term "alloy" mainly refers to the homogenous ordering in (a), while (b) would be termed a phase-separated intermetallic phase.

A hypothetical phase diagram between the constituent elements *A* and *B* are presented in Figure 8. Here we follow the multiple phase changes that occurs after having prepared an alloy of composition X_O at elevated temperature T_0 and subsequently letting it cool down to lower temperatures. We assume that we initially prepare an alloy of composition X_O at temperature T_0 (point *O* in the phase diagram). At this temperature the alloy is in a liquid state (L) with the constituents *A* and *B* randomly mixed (Figure 7a) in a solution. The overall composition is X_O. We then let the system cool, and when the temperature has dropped to T_1, the alloy is in a state where a solid of local composition X_b (point b) nucleates in the liquid, which now has a composition of X_a (point a). The volume ratio between the liquid of composition X_a and the solid of composition X_b is such that the overall composition is still X_O. When the alloy cools further to temperature T_2 (point

c), the entire system is now solid (S). Also at this point, the alloy is in the form of a solid solution (Figure 7a) between the constituents A and B of composition X_O. The area where the solid solution is stable is highlighted in the phase diagram as (A, B). When the alloy cools even further to temperature T_3 (point d), we enter a point where the solid solution is not stable anymore. Instead, two different compositional phases forms (Figure 7b), one of composition X_e (point e) and one of composition X_f (point f). Again, the volume ratio between the two phases is still such that the overall composition is still X_O.

Phase diagrams, such as the one presented in Figure 8, are not only limited to metallic alloys, but will also be of use to describe the Pd-H system later in section 4.2.

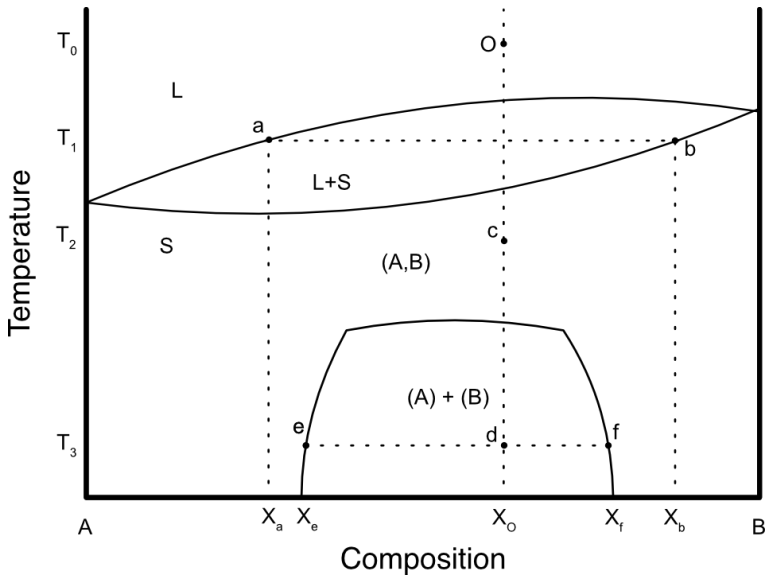

Figure 8: Hypothetical temperature-composition phase diagram for binary alloy *AB*.

4 The Palladium-Hydrogen System

The reason for the great interest in Pd for hydrogen technologies is that the metals is not only highly efficient in dissociating the hydrogen molecule already at ambient conditions on its surface, but it can also subsequently absorb the monoatomic hydrogen. When a hydrogen molecule impinges on the Pd surface, it splits into monoatomic hydrogen essentially without any energy barriers[40] - but hydrogen does not only stay on the surface of Pd. At increased hydrogen pressures, it is thermodynamically favorable for hydrogen to also reside inside the Pd lattice compared to staying in the gas phase, which means that Pd not only dissociates the hydrogen molecules - it also absorbs the resulting monoatomic hydrogen into interstitial sites of its lattice. This happens already at ambient conditions As such, Pd can act as both a catalyst for the dissociation of hydrogen *and* as a storage medium for the resulting hydrogen atoms.[40]

While the dissociation process of hydrogen on the surface is barrierless, the diffusion into the bulk is not. The diffusion of H also proceeds in different steps, first into a subsurface layer just beneath the surface and then from this subsurface layer and further into the bulk.[41] The energies of the different steps are schematically represented in Figure 9. The kinetically rate-limiting step of this process is well-established to be the diffusion of dissociated hydrogen from the surface to the first sub-surface layer.[41, 42]

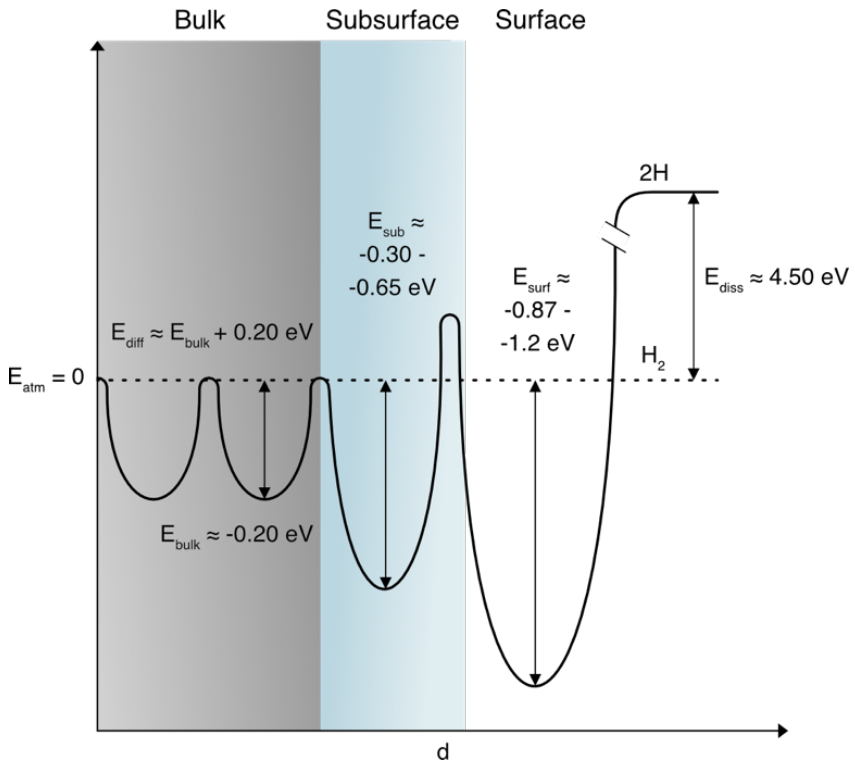

Figure 9: Energy landscape encountered by a hydrogen molecule dissociating on the Pd surface and diffusing into the bulk. E_{diss} represents the change in energy between the hydrogen molecule and dissociated monoatomic hydrogen. E_{surf}, E_{sub} and E_{bulk} represents the binding energy of hydrogen at surface, subsurface and bulk sites, respectively. E_{diff} represents the diffusion barrier for hydrogen to diffuse from one bulk octahedral site to another. Energy values are compared to a hydrogen molecule in the gas phase E_{atm}.[41-43]

When a small amount of hydrogen has diffused into the bulk of Pd, the interstitial hydrogen will be distributed in the Pd lattice as a sparsely populated solid solution called the α-phase. The interstitial hydrogen strains the Pd lattice and increases the lattice parameter up to a maximum of 3.895 Å (for the α-phase), which is slightly larger than the lattice parameter of 3.887 Å for pure Pd.[38] In the α-phase, the Pd-H system obeys Sieverts' law,

$$n_H = \frac{K_s}{\sqrt{p_{H_2}}}$$

(6)

which states that the concentration of hydrogen inside a metal, n_H, is inversely proportional to the square root of the partial hydrogen pressure p_{H_2} outside the metal by way of Sieverts' constant K_s.[44, 45] In other words, if the partial hydrogen pressure p_{H_2} continues to increase, more and more hydrogen will absorb into the Pd lattice. However, when the hydrogen pressure is high enough, Sieverts' law will break down as it will become favorable for the system to increase its lattice parameter substantially to make room for the added hydrogen – a new phase will form. The thermodynamic driving force behind this phase change is an effective attractive interaction between interstitial H atoms in the lattice (more on this in section 4.1.3). This new phase of the Pd-H system is called the β-phase or the Pd-hydride and has an (increased) lattice parameter of 4.025 Å.[38]

Even though the β-phase of hydrogen in one way or another has been known to exist since the 1920s[46], exactly how the phase transformation goes about has been a matter of great debate.[47-49] Not only can the process differ substantially between a bulk and a nano-scale system, but except for the smallest of nanoparticles, there is also large hysteresis between the hydrogen pressure for formation and decomposition of the β-phase, respectively. This hysteresis manifests as a difference in hydrogen pressure for the α-to-β phase transformation compared to the reverse transformation, where the former occurs at a higher hydrogen pressure than the latter. Different mechanics for what causes the hysteresis has been proposed throughout the years, for

example that the hysteresis is caused by energy losses due to the formation of dislocations during both α-to-β transformation as well as the reverse process.[47] However, with this explanation, it would be difficult to explain the reproducibility of hysteresis measurements on the same system, as the formation and subsequent destruction of equal dislocation networks time after time during repeated hydrogen cycling is highly unlikely.[50] A more recent theory regarding the origin of hysteresis in Pd instead involve different types of strains acting on the system during the transformation.[48, 50] In order to sort all this out, we will need to look closer at the details behind the formation of palladium hydride.

4.1 Gibbs Free Energy Affecting Interactions in the Pd-H System

In the following sections, I will briefly review the different competing interactions found to affect the Gibbs free energy and enthalpy of formation for palladium hydride.

4.1.1 Binding Energy of H in Pd

The binding energy of H in Pd depends on where in the crystal the hydrogen resides. As already mentioned, the energetically most favorable position for hydrogen is the surface of the palladium.[41, 43] However, the binding energy of hydrogen in the bulk is still favorable for the hydrogen compared to continuing being in the gas phase (∼-0.2 eV in favor of an octahedral interstitial site compared to gas phase), so the hydrogen atoms will want to diffuse into the bulk when surface and subsurface sites are occupied.[42] This

is the main thermodynamic driving force for the phase transformation in the bulk of the Pd system.

4.1.2 Strain at the Phase Boundary

Due to the larger lattice parameter of the Pd-H β-phase compared to the α-phase, significant strain will be exerted on the crystal lattice in the interface region if the phase transformation proceeds coherently, i.e. if the crystal lattice stay intact without formation of dislocations forming (see section 3.3 for the details of coherent vs incoherent phase transitions).[50] The interface-induced strain introduces an energy barrier for the growth of either phase into the other. In other words, compared to if this strain would be non-existent, a higher hydrogen pressure will be required to drive the growth of the β-phase into the α-phase to overcome the strain barrier. In the same manner, a lower hydrogen pressure will be required to drive the growth of the α-phase into the β-phase, *i.e.* the system exhibits hysteresis.[50]

The induced strain between the two phases is considered the main cause of hysteresis in an open, otherwise strain-free system that transforms fully coherently. However, this effect breaks down as soon as the phase transformation proceeds incoherently instead of coherently, as the coherent strain between the two-phase boundaries then is greatly reduced. As discussed in section 3.3, it can be energetically favorable for a system to switch from a coherent to an incoherent phase transformation if the strains involved in the former grows too large. This is exactly what happens during hydrogen absorption in the Pd-H system when the grains/crystals reach a critical size.[48, 49, 51] However, exactly how large a crystal needs to be to achieve this critical size has been highly debated.[48, 49, 51] It is well established

that for macro-scale bulk Pd, the grains are large enough to transform incoherently, i.e. dislocations are formed to relieve stress during the phase transformation.[52] For nano-scale systems like single-crystalline nanoparticles on the other hand, different critical sizes of ~40 nm up to 300 nm have been found.[48, 49, 51] The discrepancy in the calculated values for the critical size for Pd nanoparticles can mainly be attributed to which model that has been used to describe the spatial growth of the β-phase. If one assumes that the β-phase grows from the (entire) surface of the particle and inwards (a core-shell structure, Figure 10a), a smaller critical size for the crystals will follow compared to if one assumes that the β-phase grows as a "cap", *i.e.* from one end of the nanoparticle to the other (Figure 10b).[49]

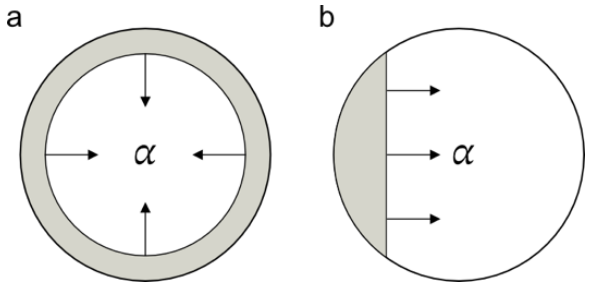

Figure 10: Schematic showing the (a) "core-shell" vs the (b) "cap" model of β-phase growth into the α-phase. In the core-shell model (a) the β-phase (in gray) grows from the surface of the particle and inwards. In the cap model (b) the β-phase grows from one end of the particle to the other.

4.1.3 Effective Attractive H-H Interactions

As we saw in section 3.1.1, adding an interstitial atom into the lattice of a host metal introduces strain on the neighboring region. This strain will also result in a locally expanded lattice around the interstitial, with a displacement

field that falls of as $\frac{1}{r^2}$.[53] With the lattice slightly expanded already, the stress added to the system if another interstitial atom would be added in the expanded region is less than if the same interstitial would be added to a non-expanded region of the lattice.[54, 55] As such, the expanded lattice around hydrogen interstitials results in an effective attractive H-H interaction that in total lowers the enthalpy of formation of the β-phase as a function of added hydrogen.[47, 48, 54, 56]

4.1.4 Electronic H-H Interactions

Working against the attractive interaction between hydrogen atoms described in section 4.1.3 is a repulsive force due to their electronic interaction. When hydrogen is added to the palladium system, the extra electron of the hydrogen atom enters the electronic bands of the host metal. The change to the enthalpy of formation of the β-phase is small for low hydrogen concentrations where the extra electron enters the 4d-band, but increases substantially at higher hydrogen concentrations where low density of states bands (like 5s) need to be filled instead.[47, 48, 53, 56] For Pd this happens when the hydrogen concentration goes above ~60%.[47]

4.1.5 External Strains

External types of strain, such as strain generated by substrate clamping, can also affect the β-phase formation enthalpies. This is especially pronounced for nano-sized systems, such as thin films, due to their large substrate-surface-to-volume ratio. It is well-established that high stresses are generated in thin films of Pd on hard substrates that feature good adhesion during

hydrogenation due to the compressive forces the substrate generates on the expanding palladium. As a consequence of this clamping, hysteresis increases.[57-60] Wagner and Pundt have also demonstrated that substrate clamping of Pd thin films leads to a lower critical temperature for the α-to-β transition, *i.e.*, that the coherent phase transition is stable at lower temperatures compared to a non-clamped system.[57] Here it is also shown that the substrate-induced stress increases with lower thickness of the studied films, and that this effect is more pronounced for coherent (compared to incoherent) α-to-β phase transitions.[57] In a direct comparison between PdAu thin films (high degree of substrate clamping) and PdAu nanoparticles (low degree of substrate clamping), Bannenberg *et al.* have confirmed both the increased hysteresis and the more stable coherent phase transition of the thin film compared to the nanoparticles.[61]

When it comes to kinetics, density functional theory calculations have shown that compressive strain leads to a decrease of hydrogen diffusion through bulk Pd compared to the unstrained case.[42]

4.2 The Pd-H Phase Diagram

Taking all the effects of section 4.1 together, we are finally ready to write the full enthalpy of formation for the α- to β-phase transformation

$$\Delta H_{\alpha-\beta} = \Delta H_{site} - \Delta H_{elast} + \Delta H_{elec} + \Delta H_{int} + \Delta H_{str}$$

(7)

where ΔH_{site} is the change of enthalpy of the H atom inhabiting an octahedral bulk site compared to remaining in the gas phase (the difference in this enthalpy for α- and β-phase is negligible[48, 56]), $-\Delta H_{elast}$ and ΔH_{elec} are the hydrogen concentration dependent attractive H-H and repulsive electronic interactions, respectively, ΔH_{int} represents the energy barrier generated from the interface strain between α- and β-phase in the case of a coherent phase boundary and ΔH_{str} represents other strains, such as surface tension and clamping.

For bulk Pd, the phase transition from α- to β-phase (and vice versa) proceeds incoherently, as we already established in section 4.1.2. This means that $\Delta H_{interface}$ is negligible. For bulk Pd we can also generally approximate $\Delta H_{str} \approx 0$, which means that for bulk Pd we get

$$\Delta H_{bulk} = \Delta H_{site} - \Delta H_{elast} + \Delta H_{elec}$$

(8)

Pressure-composition isotherms for bulk Pd, which relate the partial hydrogen pressure to the concentration of absorbed hydrogen, can be constructed using the Van't Hoff relation[48]

$$\frac{1}{2} ln\, p = ln\left(\frac{x}{1-x}\right) + \frac{\Delta H_{bulk}}{RT} - \frac{\Delta S}{R}$$

(9)

where p is the partial hydrogen pressure and x is the H/Pd composition ratio. However, the H_2 pressure-composition isotherm calculated by equation (9) has some unphysical parts. The Van't Hoff relation does not explicitly enforce the equilibrium stability conditions of positive isothermal compressibility and equal chemical potential for different phases. These conditions can however be enforced by using the Maxwell construction on the resulting pressure-composition isotherm (Figure 11).[17, 48] Hence, for the H/Pd concentration $c_\alpha < x < c_\beta$, two different phases, one of concentration c_α and one of concentration c_β forms while the pressure is kept constant. Interestingly, the simple strain free model of equation (8) and (9) effectively reproduces desorption isotherms of bulk Pd.[48] However, to accurately reproduce bulk Pd absorption isotherms, some strain needs to be included in the model.[48, 52]

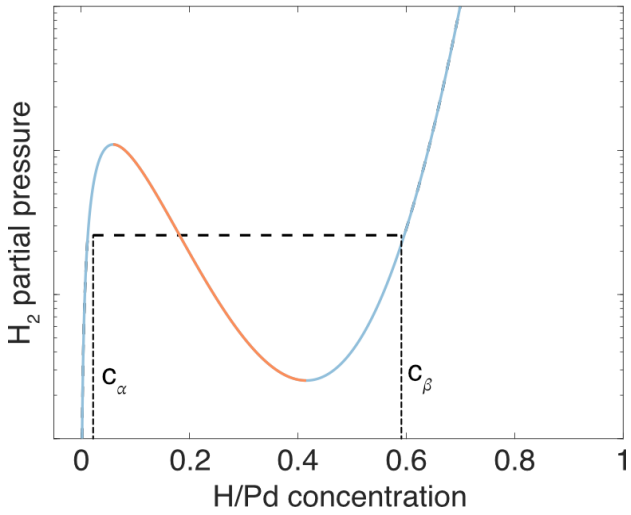

Figure 11: Schematic representation of pressure-composition desorption isotherm adapted from Griessen *et al.*[48] The red part of the isotherm is unphysical for a stable state as it implies that pressure is decreasing with increased volume (increased H/Pd concentration). This condition (and the condition of equal chemical potential for different phases) can be enforced by use of the Maxwell construction[17, 48] (horizontal, dashed line) which yields that for the H/Pd concentration $c_\alpha < x < c_\beta$, two different phases, one of concentration c_α and one of concentration c_β forms.

This means that we finally can construct the phase diagram of the bulk Pd-H system for each temperature T (Figure 12). For every temperature below the critical temperature T_c, hydrogen sorption will follow a temperature-specific pressure-composition isotherm (dashed line in Figure 12) through the α-phase up to the critical concentration c_α. At this hydrogen concentration, the β-phase with a local concentration of c_β will nucleate across the system. From now on, the β-rich regions will grow at the expense of the α-rich regions until the hydrogen concentration of the entire system is c_β and the phase transformation is complete, all while the hydrogen pressure is kept constant. At temperatures higher than T_c, the α- and β-phase are

indistinguishable from each other and cease to exist. The lattice parameter of the Pd-H system then instead increases proportionally with increased hydrogen concentration.

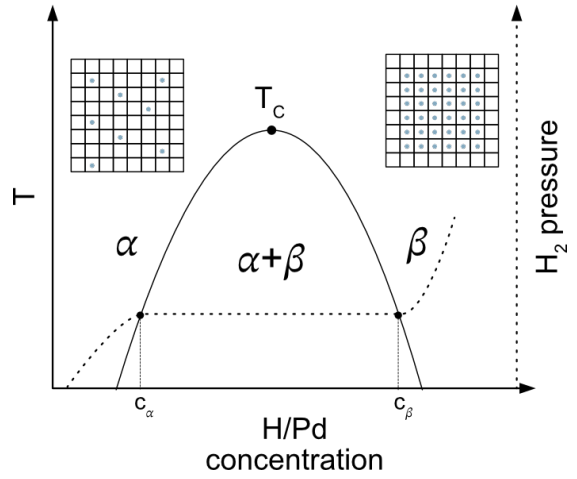

Figure 12: Schematic of the bulk Pd-H phase diagram. At low hydrogen concentrations, the system is in the α-phase where hydrogen forms a dilute solid solution in the Pd lattice. As the external hydrogen pressure increase (dashed line), the hydrogen concentration in the metal increases up to the (temperature specific) critical concentration c_α. Now we enter the two-phase coexistence region where β-rich regions of concentration c_β grow at the expense of the α-rich regions of concentration c_α until the entire system has transformed to the β-phase. The area between c_α and c_β (solid line) is called the miscibility gap and decreases with increased temperature until it disappears at the critical temperature T_c.

4.2.1 The Pd-H Phase Diagram for a Nano-Sized System

The main differences from equation (8) when the size of the system is reduced are the resurgence of the ΔH_{int} and ΔH_{str} terms of equation (7). When the size is reduced, we approach a critical size below which

nanoparticles and thin films transition from the α- to the β-phase coherently instead of incoherently. When this happens, ΔH_{int} becomes significant, as explained in section 4.1.2. The ratio between the surface in contact with the substrate compared to the total volume of the system also increases as we downscale the system. Hence, substrate-induced strains (as explained in section 4.1.5) and consequently ΔH_{str} may also become considerable. Taken together, this means that absorption pressures and hysteresis generally are increased for nano-sized systems compared to macroscopic bulk, as exemplified by Griessen *et. al.* when comparing the results found in the literature between single-crystalline Pd nanoparticles and Pd bulk.[48] As the energy barrier of ΔH_{int} is proportional to the volume of a coherent system[50], the hysteresis becomes a function of crystallite size below the critical size and as such hysteresis is reduced for smaller particles to eventually essentially disappear.[11, 48, 49]

4.3 Alloying

A way to engineer the intrinsic strain level of a metallic system, such as Pd, is through alloying. Alloying has been employed successfully many times to alter both the thermodynamics and kinetics of the Pd-H system.[7, 62-71] One of the most studied nano-sized Pd alloy systems is PdAu, and here it has been shown that the added Au atoms both reduce hysteresis and speed up kinetics.[66, 72-74] The reduction in hysteresis is attributed to an expansion of the lattice parameter of the PdAu alloy due to the larger lattice parameter of Au compared to Pd.[65, 66, 75] This acts as a "pre-straining" of the Pd lattice and thereby lowers the relative strain induced by hydrogenation and consequently decreases the hysteresis. The speed up of the kinetics can be

traced to a reduction of the rate-limiting energy barrier for diffusion of hydrogen from surface to subsurface sites.[73]

In contrast to expanding the lattice by alloying with Au, one can also contract the lattice by alloying with an element that has a smaller lattice parameter than Pd, such as Cu. The resulting increased compressive strain compared to pure Pd consequently raises the absorption pressure – in line with what we have seen so far of how strain influences hydrogenation properties.[64] However, in contrast to PdAu, alloying with Cu also substantially increases desorption pressures, which results in a reduced hysteresis for this system as well.[64]

4.4 The Role of Defects

The presence of different kinds of defects in the Pd system significantly alters and complicates the study of palladium's interaction with hydrogen. It is well known that hydrogen is attracted to different defect sites, such as vacancies[76], dislocations[77] and grain boundaries[78] due their stronger binding energy.[79] Also, when the strains during phase transition grow large enough for the α/β phase transformation to change from an elastic, coherent transformation to a plastic, incoherent transformation - large amounts of dislocations may be generated in the process.[57-60, 80-82] This significant alteration of the microstructure may have a substantial impact on the hydrogenation properties of the system, as we will see later in this chapter.

The role of defects regarding the kinetics of the Pd-H system is at first glance contradictive. The lower energy sites of dislocations and grain boundaries should act as traps for hydrogen and consequently lower the diffusivity of

hydrogen through the metal. Accordingly, a lower diffusion constant is actually measured for Pd samples with higher degrees of dislocations and grain boundaries compared to defect-free samples.[47, 79, 80] However, this effect is most pronounced in the very low-concentration α-regime (< 0.001 H/Pd ratio, < 0.1 mbar H_2 partial pressure). When the hydrogen pressure is increased (> 0.01 H/Pd ratio, > 0.1 mbar H_2 partial pressure), the deepest (lowest energy) traps are already saturated and higher energy sites has to fill instead. When this happens, pathways that include a range of different energy sites (such as defects like grain boundaries and dislocations) that are both higher and lower in energy than pathways with sites of more constant energy (such as a pathway through a defect-free crystal) may overtake the latter in terms of diffusion, as the former effectively gets a reduced activation energy for diffusion.[83, 84] Experimental verifications of Pd with higher defect densities having faster absorption kinetics than Pd with lower defect densities have been confirmed for nanocrystalline Pd films vs single-crystal films[83], as-deposited (and as such, defect-rich) magnetron sputtered vs annealed Pd thin films[85] and for highly-nanocrystalline Pd nanoparticles[10]. Also, increased strain has been found to act detrimentally for diffusion by reducing diffusion coefficients compared to the un-strained case.[42] Hence, as defects such as dislocations may relieve stress in crystals, this could also be one of the reasons for the accelerated kinetics.

Regarding hysteresis, in a small (either a nanoparticle or a thin film below their respective critical size for coherent phase transformation), defect-free system – we would expect a large hysteresis between absorption and desorption pressures due to the large strain put on the system by either the α-β phase boundary (in the case of a free nanoparticle) or the substrate clamping (in the case of a thin film). When strain is alleviated from the

system, for example by plastic deformation, we expect absorption pressures and hysteresis to decrease. This has been exemplified by Alekseeva *et. al.* where it was shown that the more grain boundaries a Pd nanoparticle has (characterized by the total grain boundary length inside the particle), the more absorption pressures and hysteresis decrease.[9] However, this effect is the most pronounced for high-angle grain boundaries. The same effect was not seen for more closely packed twin boundaries. This makes sense from the view that high-angle grain boundaries provide more room for grains to expand during hydrogenation than more closely packed grain boundaries, *e.g.* twin-boundaries.[9]

Until now we have mainly focused on how *new* defects are generated and the effect they have on the hydrogenation properties of Pd, but the hydrogenation process can also alter an already existing defect network as well. It is well established that the mobility of dislocations increases in the hydride state[47, 80] and dislocations and (closely packed) grain boundaries have even been found to completely "heal" after hydrogenation.[10, 86] Wagner and Pundt have investigated the stress evolution during hydrogenation of three thin-film Pd samples with different defect densities.[57, 58] During the initial part of the hydrogenation (before major plastic deformation), the highest stress levels were found in the defect-free single-crystalline sample, while the lowest stress levels were found in the sample with pre-existing dislocations. These dislocations could then move during hydrogenation to relieve the rising stress levels. The highest final stress (after major plastic deformation) was found in the sample with the highest density of pre-existing grain boundaries. The high stress level in this sample was attributed to dislocation pile-up at the many grain boundaries hindering stress relaxation.[57, 58] On the other hand, the lowest final stress levels were found in the (nominally) single-crystalline

sample where stress relaxation through plastic deformation is the most efficient.[57]

As a final note on defects, figuring out the exact strain and defect density state, and how these interact in any system beyond small, defect free and single crystalline nanoparticles, is highly non-trivial. This is exemplified by bulk palladium. As we have already established, the hydride phase transformation is incoherent in bulk, the support plays a minimal role and the system is generally assumed to be stress-free (by the assumption that it can freely expand upon hydrogenation).[57] This would imply a hysteresis-free system, yet hysteresis is always observed.[47, 48] Traditionally, this has been explained by the formation and movement of dislocations during both absorption and desorption.[47] More recently, an alternative suggestion have been explored in regards to the last assumption that palladium is free to expand upon hydrogenation. Griessen *et al.* have shown that the desorption of hydrogen from bulk Pd follows the trend expected from a fully stress-free system but that the absorption in contrast proceeds as in a strained system.[48] The observed hysteresis in bulk can in other words be explained by stress that is only present during absorption and not during desorption. To this end, effects, such as grain-boundary or dislocation pinning that introduce strain during β-phase growth, could provide the mechanistic explanation for this asymmetry between hydrogen absorption and desorption.[87] The truth is probably somewhere in between, where an intricate interconnection between strain and the formation and movement of dislocations work together to create the observed hysteresis at all levels of the Pd-H system.

4.5 The Big Picture

As the final words of this chapter, we have now established the critical role that strain and defects have on the thermodynamic and kinetic properties of the Pd-H system. In general, more strain in the system leads to increased absorption pressures and wider hysteresis. The hydrogenation induced strain can be alleviated by plastic deformation, either through the creation (of new) or the movement of (already existing) dislocations. These and other defects typically enhance the kinetics of hydrogen through the Pd lattice by providing alternative pathways as well as lowers the hydrogenation hysteresis compared to a highly strained system. However, as defects may also heal during hydrogenation, the opposite trends may also be observed. If it is favorable for the system to get rid of defects or generate new ones depends on the initial strain and defect state of the system. Beside defects, we can also engineer the strain state of the Pd system by alloying. Alloying unlocks possibilities that are unreachable by using Pd alone, but also add complexity by introducing alloy composition as an additional variable beside all the parameters already discussed in this chapter.

5 Experimental Methods

When allowing for alloying and defect engineering of the Pd-H system, we are suddenly faced with a huge parameter space of almost unmanageable proportions. For example, with defect engineering, reproducibility is an issue where it is almost impossible to fabricate two samples with equal defect states. For alloying, the full composition space for binary and ternary Pd alloys alone is beyond what anyone could study during a lifetime. Add to this that, for example nanoparticles, display a high degree of individuality in terms of structure between particles on the *same* sample, it quickly becomes apparent that large amount of data is necessary in order to draw statistically relevant conclusions from experimental measurements on these systems. Fabricating and measuring the required number of samples would thus quickly become unviable if a new sample had to be made for each new defect or alloy system to be investigated.

As an alternative, if one instead would be able to screen many systems at once on a *single* sample – for example different degrees of deformation or many different alloy compositions – one would not only greatly reduce the number of samples, but also experiment-to-experiment uncertainties could be eliminated. In the following sections, we will go through the different methods that allow us to do exactly this, *i.e.*, study alloy and defect engineering at the individual nanoparticle level on a single sample.

5.1 Single Particle Plasmonic Microscopy

To study nanoparticles at their individual level, we make use of an effect called localized surface plasmonic resonance (LSPR). This effect has been

utilized to great success in the recent two decades to, among other applications, study the catalytic and sensing properties of nanoparticles to a high level of detail.[7-11, 61, 64-66, 74, 88-105] In brief, the LSPR effect is based on the propensity of electrons in the conduction band of a metal to oscillate when experiencing the alternating electric field of an irradiated propagating light wave. If the size of the metallic system is reduced to a size comparable to the wavelength of the light, such as is the case for a nanoparticle, the free electron cloud of the entire particle will oscillate in sync with the light (Figure 13a). This is a resonance effect (the simplest analogy being a mechanical harmonic oscillator) where the strength of the response is wavelength dependent and is determined by the material composition, size, geometry and dielectric environment of each nanoparticle. A change to any of these parameters will generally result in a (measurable) shift in the plasmonic response, *e.g.* its frequency or intensity.

In the case of palladium and hydrogen, the LSPR for Pd-based nanoparticles shift both in terms of frequency (a red-shift) and intensity (a decrease) when the Pd particle absorbs hydrogen.[88, 106, 107] The reason for this is due to the absorbed hydrogen changing the dielectric function of the system by way of altering the density of states as well as enabling more interband transitions, which in turn leads to the before mentioned red-shift and intensity decrease of the plasmonic resonance.[106, 108] This change can be probed with, for example, spectroscopic extinction measurements or intensity based scattering measurements (Figure 13b).[9, 10, 64-66, 74, 109-111] We will focus on the latter method – and more specifically – intensity based measurements in a back-scattering dark-field microscopy setup. In this type of measurement, high-angle illumination of the object is employed as to only allow scattered light from the object to be collected by the objective lens (Figure 14a). The

light used for illumination is reflected at a high angle and is therefore not collected.

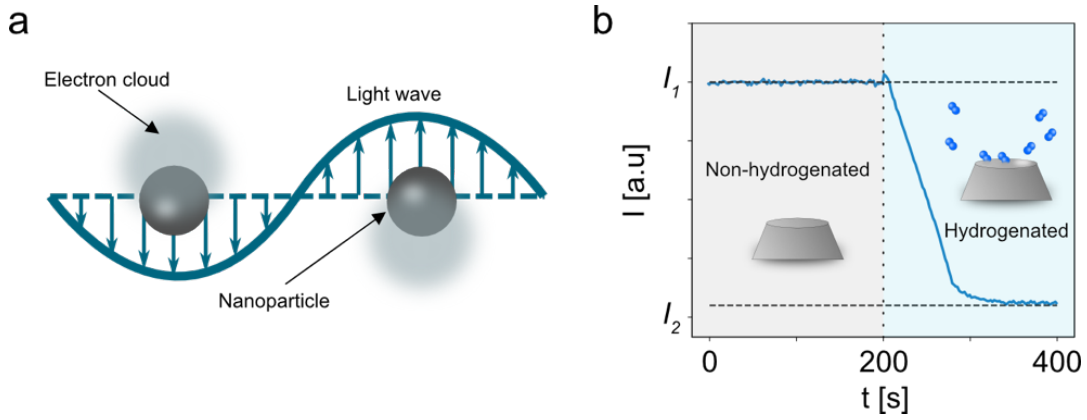

Figure 13: (a) Schematic of the principle behind localized surface plasmon resonance (LSPR). A propagating light wave induces a synchronized oscillation of the free electrons in metallic nanoparticles. (b) Example of the hydrogenation-induced LSPR intensity drop of a Pd nanoparticle. Before hydrogenation the intensity is at level I_1 and after hydrogenation the intensity has dropped to level I_2.

The diffraction limit of light limits the minimum resolvable feature size using optical wavelengths. As the size of our nanoparticles (~100 nm) is below the diffraction limit for all visible wavelengths, this translates to an inability to distinguish the number of particles that gives rise to a specific diffraction limited spot in a dark-field scattering measurement using visible light (Figure 14b). However, if we can place the particles with enough separation, for example with electron beam lithography (more on this in section 5.2), we can be certain that each diffraction limited spot is the result from light scattered from a single nanoparticle. How this might look through a dark-field microscope is presented in Figure 14c. The measurement of the hydrogenation properties of single Pd-based nanoparticles is then just a

matter of tracking the intensity of each diffraction limited spot during a hydrogenation process.

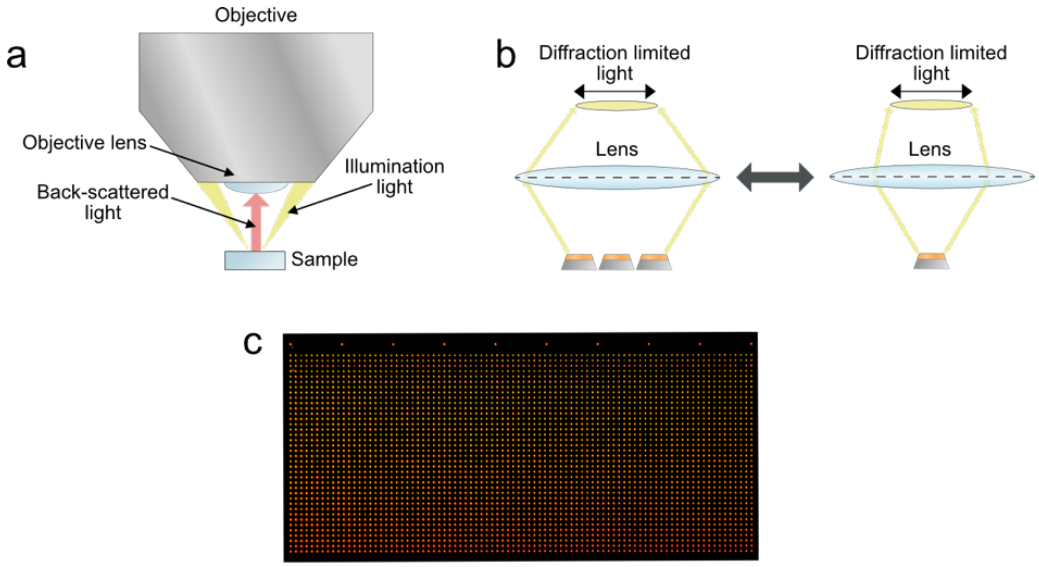

Figure 14: (a) Schematic of the principle behind back-scattering dark-field microscopy. The irradiated light exits the objective at a high angle, which means that only the back-scattered light from the sample reaches the objective lens. The incident light is reflected away due to its high incident angle. (b) Schematic of the diffraction limit of visible light, as applied to imaging of nanoparticles. A group of particles vs. a single particle are spatially undistinguishable as they both give rise to diffraction limited spots of equal size. (c) An array of a spatially separated PdAu nanoparticles as viewed through a dark-field microscope. Each diffraction limited spot of light is the result of the light scattering from a single nanoparticle.

In order to measure the hydrogenation properties of individual Pd-based nanoparticles, I have built a custom experimental setup to be used together with a dark-field microscope (Figure 15). This setup consists of a gas-tight chamber for the nanoparticle samples with optical access through a glass window. An inlet and an outlet allow exchange of the gas environment and

are controlled by automatic valves. To the outlet either an exhaust pipe or a vacuum pump can be connected to allow for continuous flow or vacuum background (minimum pressure in the measurement chamber ~1 μbar) experiments, respectively. Different gases (*e.g.,* Ar, H_2 and O_2) are available and supplied to the inlet through mass-flow controllers (MFC's) which allow us to control their individual flow rates. All gases can be mixed in the inlet piping before introduction into the measurement chamber. A heating stage beneath the sample and heating tape mounted on the inlet piping allows for measurements at elevated temperatures. The optical signal generated by the sample is collected through the dark-field microscope by either a CMOS or an electron-multiplying CCD camera. The system is fully automatic and controlled by scripts through a custom software to allow for maximum reproducibility and to minimize operator-induced experiment-to-experiment errors.

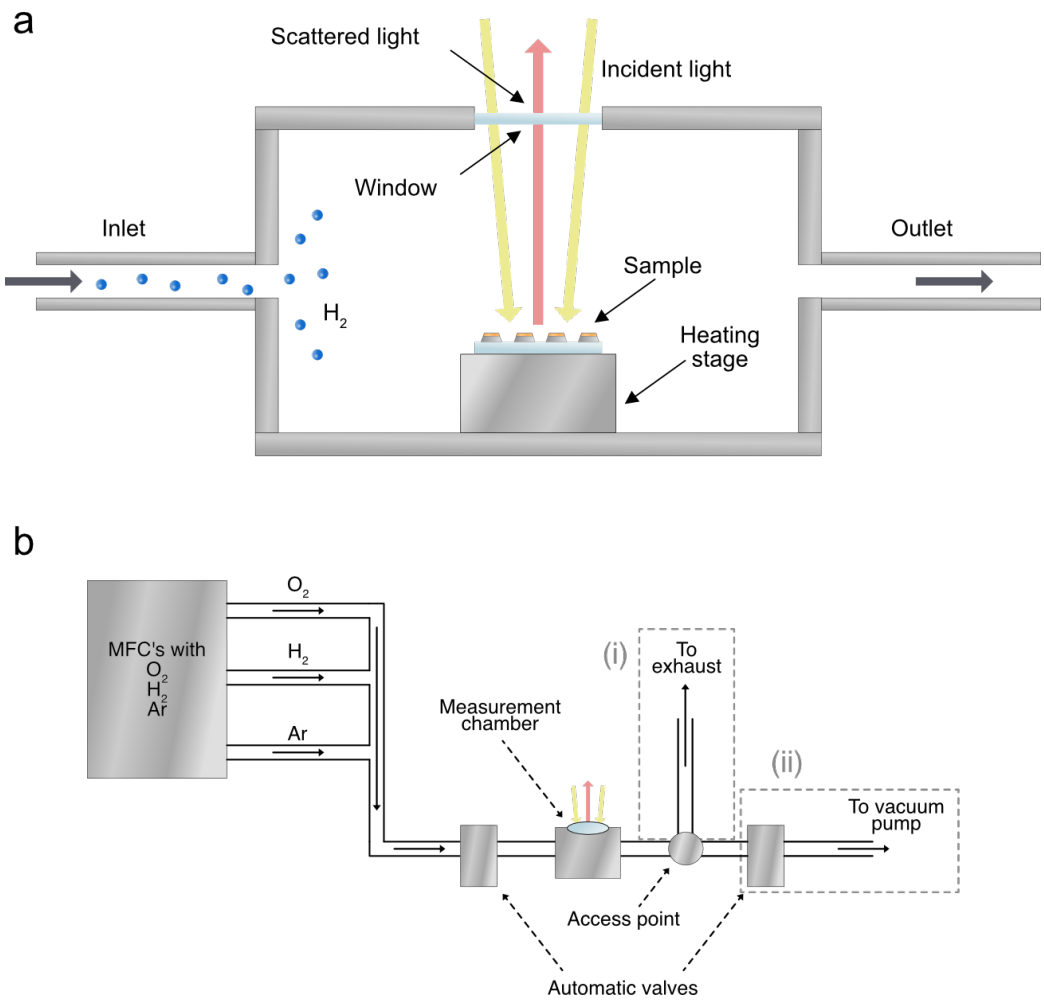

Figure 15: (a) Schematic of my plasmonic gas sensing chamber. The samples are placed on top of a heating stage inside a gas-tight measurement chamber with optical access through a top-mounted glass window. An inlet and outlet provide gas exchange through automatic valves. (b) Schematic of my full gas sensing setup. MFC's provide controllable gas flows that are mixed in the inlet piping. An automatic valve controlls when the gas is introduced into the measurement chamber (a). An access point provides the choice between i) continous flow experiements where the gas is fed to the ventilation exhaust or ii) a second automatic valve which leads to a vacuum pump, which is used for kinetics experiments in vacuum.

To summarize, with the use of our custom built dark-field plasmonic microscopy setup, we can measure the hydrogenation properties of individual Pd-based nanoparticles through their diffraction limited scattered light, even though the particles themselves are way too small to resolve using optical light. In Figure 16, a darkfield image of a representative array of PdAu is shown as seen through the setup. Particles of 2.5 μm separation is easily distinguishable, and with the full field of view of 380 x 380 μm (as decided by the microscope objective and size of camera sensor), a theoretical limit of ~ 23 000 individual particles imaged at once is reached – showcasing the potential of the method.

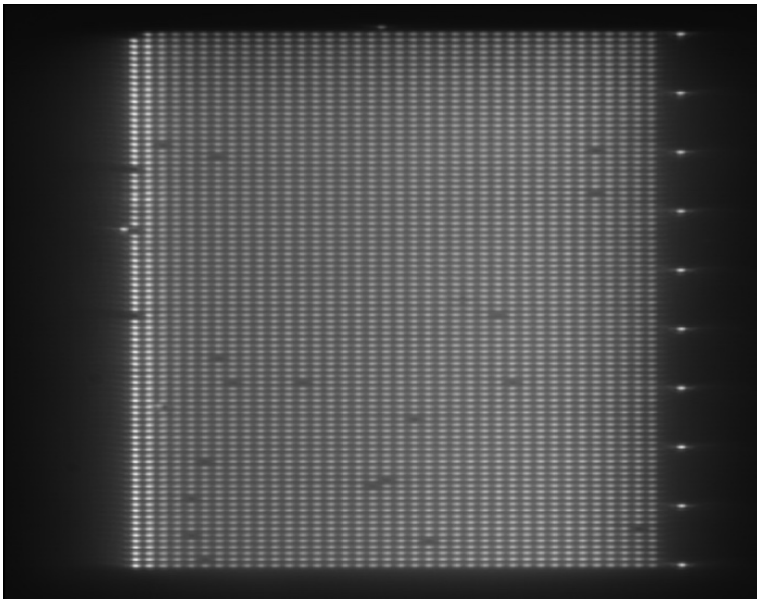

Figure 16: Representative image of an array 38 x 88 PdAu nanoparticles as imaged through the microscope objective. The close-packed particles have a particle-to-particle distance of 2.5 μm.

5.2 Microshutter Nanofabrication

By utilizing the single particle plasmonic microscopy technique described in section 5.1, we would be able to screen a large alloy composition parameter space in a single measurement if a sample could be made were the composition of different alloy nanoparticles varies across the sample. For this purpose, the microshutter nanofabrication method was developed (Figure 17).

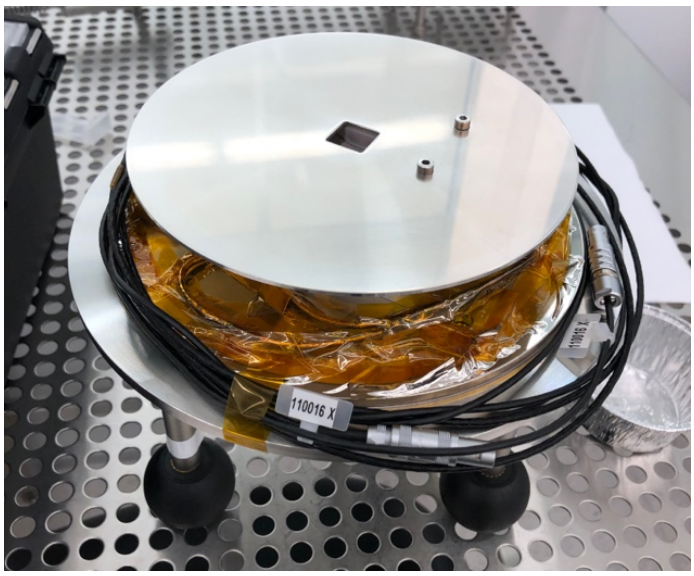

Figure 17: Image of the microshutter device made to be used together with a Lesker PVD225 e-beam physical vapor deposition system.

Before we go into the details of the microshutter fabrication method, we need to describe the general foundation for how we nanofabricate alloy nanoparticle array samples on a surface to use together with the single particle plasmonic microscopy technique described in section 5.1.[112] This approach is based on the subsequent deposition of thin films of different metals whose thickness defines the final alloy composition through a

supported, prefabricated nanolithography mask. This mask defines the size and position of the nanoparticles. The fabrication of the mask is outlined in Figure 18a and can be summarized as follows: I-II) a substrate wafer (*e.g.* Si, SiO_2 or sapphire) is prepared and spin-coated with an electron sensitive resist. The polymers in this type of resist are sensitive to electron exposure which breaks their internal molecular bonds to make exposed areas selectively soluble to a specific developer solution. To this end, the spin-coated wafer is exposed to electrons (III) by use of an electron-beam lithography (EBL) system which defines the structures of the mask. The sample is finally placed in a developer solution which dissolves the resist in the areas exposed to the electron beam (IV) – the mask is complete.

The next step of the fabrication is the subsequent deposition of different metals through the mask. This is done by evaporation of thin films of the desired metals by an e-beam physical vapor deposition (PVD) system. The metals are deposited layer-by-layer (Figure 18b), and the ratio between the layer thickness for the different metals defines the composition of the final alloys. After the PVD step, the mask is removed in a lift-off step and the sample is annealed to form the final, alloyed nanoparticles. This annealing process is based on the principle of thermodynamically driven atomic mixing of alloy components, which can occur far below the respective melting temperatures of the constituent metals.[112] As such, homogeneous alloys can form, despite the low temperature, provided that alloying is thermodynamically favorable and that sufficient time is provided.[112]

This fabrication method has been used to great success[61, 64-66, 74, 112-114], but evidently has the drawback that a new sample must be made for each new alloy composition. The microshutter alleviates this limitation. The tool itself

(Figure 17) is a custom-built sample holder for the PVD system and introduces a moveable piezo-controlled microaperture between the sample and the metal source (Figure 18c). Hence, when the aperture moves across the sample it defines both the area where the metal is deposited and the final thickness of each metal layer. In this way, particles of varying alloy compositions can be fabricated on a single sample by moving the aperture across the sample during thin film evaporation. The demonstration of this technique and its application for plasmonic-based hydrogen sensing is the focus of **Paper I**.

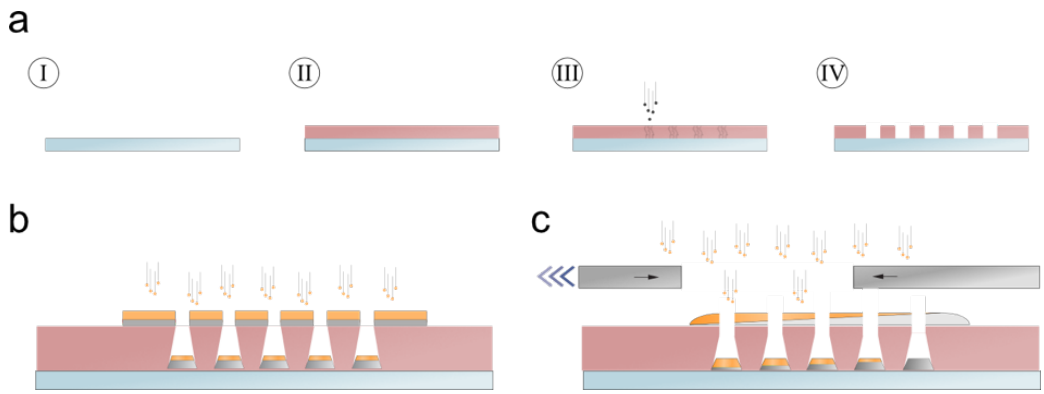

Figure 18: (a) Schematic of the fabrication process of a nanoparticle nanolithography mask using EBL. I-II) A substrate wafer (*e.g.* Si, SiO_2 or sapphire) is prepared and spin-coated with an electron-sensitive resist. III) The wafer is exposed to electrons using an electron-beam lithography system. This defines the features of the mask. IV) The electron-exposed areas are a dissolved in a developer solution. (b) Metallization of the sample. Metal films are subsequently deposited on top of the sample and nanoparticles are formed inside the holes of the mask. (c) Microshutter metallization of sample. Metal is only deposited at the area defined by the moving micro-aperture, which results in controllable thickness gradients of the deposited metal films across the sample.

We will now look closer at some important details of the microshutter tool. One of the main limiting factors in terms of both the spatial and compositional resolution of the tool comes from how well the sample substrates can be diced. The reason for this is related to how samples are mounted in the microshutter. At the PVD step of the fabrication process, the sample (with its prefabricated mask) is mounted in a fixed slot inside the microshutter (Figure 19a). As the dimensions of this slot are fixed, this means that the sample must fit perfectly inside the slot for maximum spatial and compositional resolution during the metal deposition. To demonstrate this, we can imagine that the sample is slightly smaller than the slot. This results in a small gap forming between the sample and the walls of the slot (Figure 19b), and translates to an uncertainty between the relative position of the aperture and the particle mask. To showcase how important this can be, a schematic of a representative nanoparticle mask together with the positions of the blocking edge of the aperture at each deposition step is presented in Figure 19c. The row-to-row distance between particle rows in the mask in this example is 2.5 μm and the aperture is programmed to stop in between every row. This means that if the sample is more than 2.5 μm smaller than the slot, we can't guarantee that the blocking edge of the aperture will be positioned correctly relative the particle mask on the sample. From this demonstration it is evident that high-precision dicing of the sample substrate is critical. Exactly how much the size of the sample and the slot can differ depends on the nanolithography mask – the closer the features that should have different compositions are too each other, the more of a high-precision fit is needed.

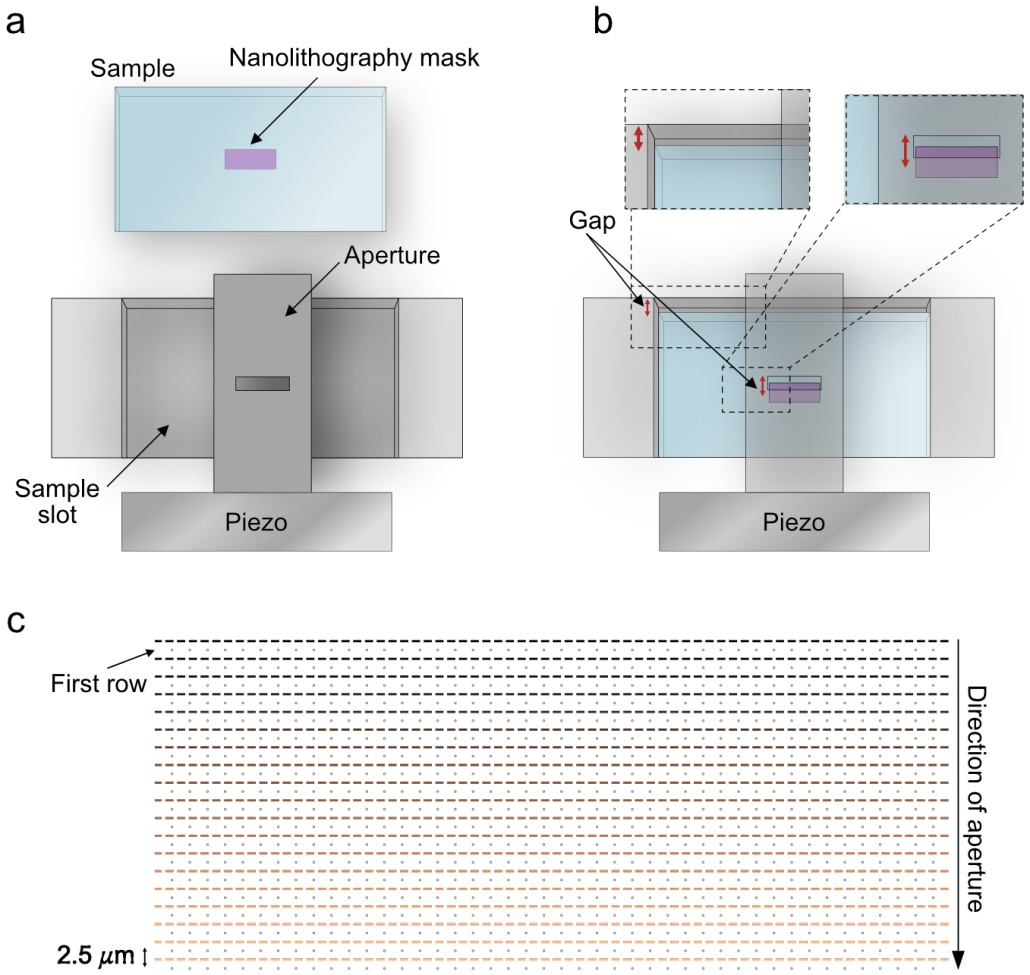

Figure 19: (a) The sample slot in the microshutter tool and the sample before mounting. (b) The mounting of a sample slightly smaller than the sample slot results in a gap forming between the sample and the slot wall (red arrow in the left magnified area). This leads to an uncertainty of the position between the microshutter aperture and the nanolithography mask (red arrow in right magnified area). (c) Schematic of a representative nanolithography mask together with the calculated position of the blocking edge of the aperture (dashed lines) in each deposition step. The aperture moves from dark to light colors.

To facilitate the necessary high-precision substrates described in the last paragraph, a time-consuming dicing solution of the substrates had to be used.

As a substrate is diced, the part of the diamond blade that experiences the most wear is the edge of the blade. This means that the use of a blade shared with other uses of the saw was not an option, as the settings of the saw that yielded a good fit at one dicing session did not yield the same result the next time. This was due to the blade being worn down by other users in between the sessions. To limit the effect of the wear on the edge of the blade, two wafers were waxed together where the bottom wafer served as a sacrificial wafer (Figure 20). This increased the distance between the worn-prone edge of the blade and the main substrate (Figure 20b). Taken all together, this process resulted in increased precision and reproducibility of the sample substrates, but the overall processing time increased due to the need for cleaning the wax of the main substrate after dicing.

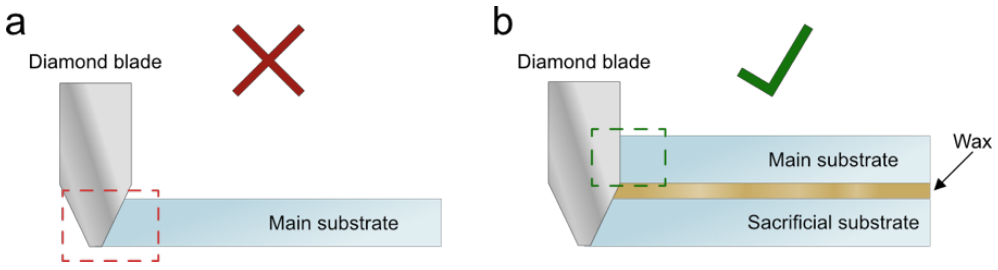

Figure 20: The dicing process of microshutter substrates. (a) Direct dicing of the main substrate lead to low reproducibility due to the wear of the blade edge (dashed red rectangle), which means that even though the same settings were used at repeated dicing sessions, the size of the samples were not consistent. (b) Using a sacrificial substrate during the dicing lifted the main substrate above the most wear-prone edge of the blade and thus raised it to a more (dicing-to-dicing) stable position higher up on the blade (dashed green rectangle). This lead to improved precision and reproducibility.

5.3 Nanoindentation

In the former section, I described how we can fabricate samples that allow us to control the composition of alloy nanoparticles at the single particle level. In the final section of this chapter, we will briefly introduce a method to instead control the defect density of our particles at the individual level - nanoindentation. This is motivated by the fact that beside the two extremes of fabricating particles with a very high or a very low density of defects, it is very difficult to systematically and reproducible fabricate particles with a controllable amount of defects. Instead, nanoindentation (Figure 21) can be used post-fabrication to systematically deform individual nanoparticles and thereby introduce defects via plastic deformation.[25, 27, 29, 115]

The nanoindenter we used (Bruker Hysitron PI85) uses a three-plate capacitive design to apply load and measure displacement simultaneously. This is done by way of an AC signal being applied each to the top and bottom capacitive plate respectively (Figure 21a). The sum of these signal is read out at the middle plate, to which the diamond tip of the nanoindenter is also attached. When a DC signal is applied to the lower plate, the middle plate with the tip is attracted downward, and as such the strength of this DC signal also defines the load of the tip (Figure 21b). At the same time, the sum of the AC signals from the top and bottom plate changes according to the displacement of the middle plate (Figure 21b). Hence, the total load-to-displacement can be extracted accordingly from the DC signal amplitude and the AC signal phase change respectively. The minimum resolvable displacement and load is < 1 nm and < 1 μm respectively.

We then used the nanoindenation technique to systematically nanoindent individual Pd nanoparticles to different degrees (nominally 5 nm, 10 nm, 15 nm, 20 nm, 25 nm, 30 nm, 35 nm and 40 nm below their nominal thickness of 60 nm). Together with the single particle plasmonic microscopy technique described in section 5.1, this allow us to investigate how different degrees of deformation influence the hydrogenation properties of individual Pd nanoparticles, which is the focus of **Paper II**.

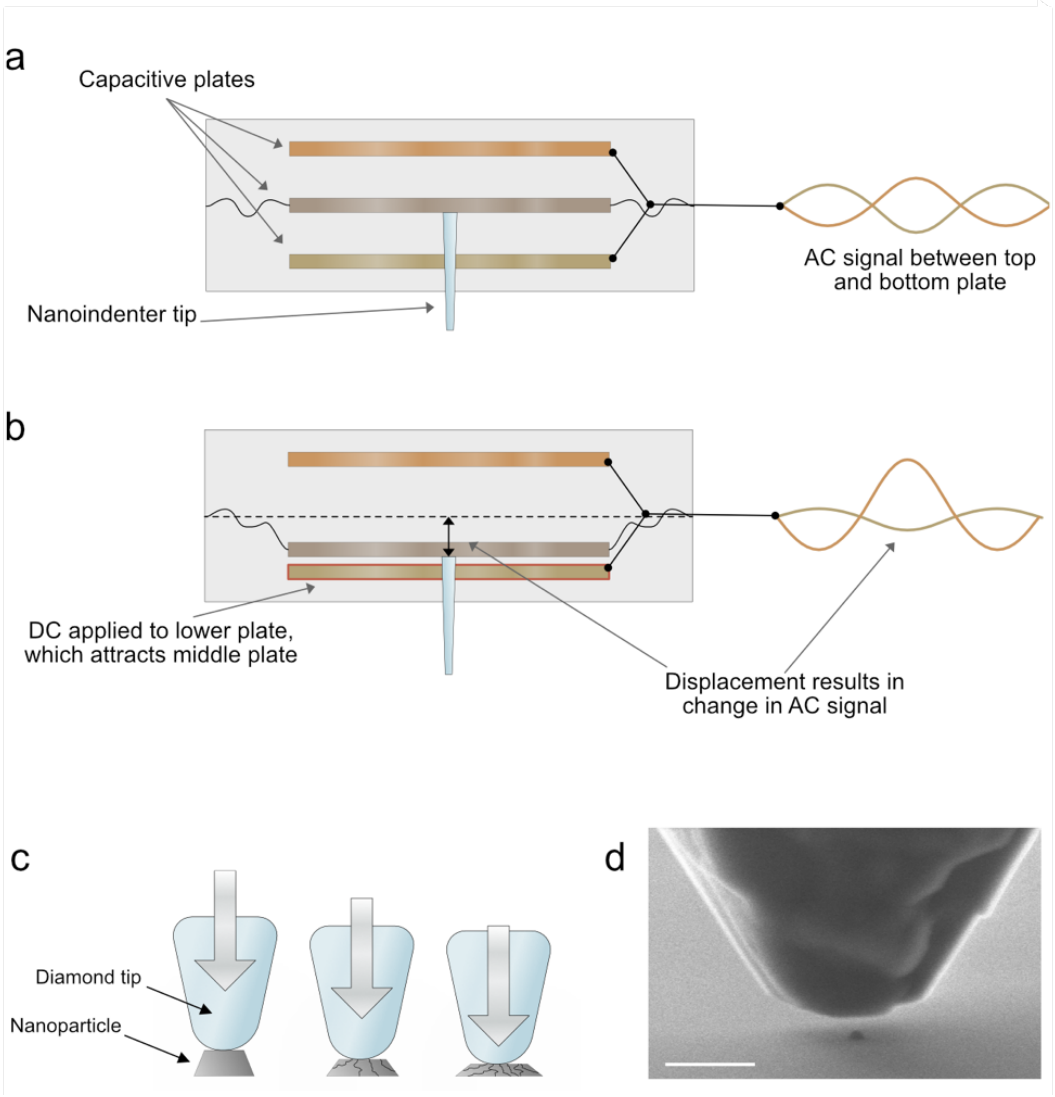

Figure 21: Nanoindentaion process of individual nanoparticles. (a-b) Schematic showing the working principle of the nanoindenter. An AC signal between the top and bottom capacitive plates are used to measure the displacement when a DC signal (the amplitude of which defines the applied load) is used to attract the middle plate (and accordingly, move the tip downward). (c) Schematic showing the process of deforming a single nanoparticle with the diamond tip of the nanoindenter tool. (d) SEM image of the diamond tip and a Pd nanoparticle belwo it just before indenation. Scale bar is 1 μm.

6 Outlook and Conclusions

As the first conclusion of this thesis, we have demonstrated the use of a piezo-controlled microshutter device that enables the fabrication of supported nanostructure surfaces with compositional gradients, with composition control down to the single nanoparticle (**Paper I**). Additionally, we have demonstrated the use of this technique to measure the plasmonic response arrays of AuAg, AuPd, and AgPd alloy nanoparticles as a function of composition. Also, the PdAu alloy sample was used in hydrogen sorption experiments to simultaneously screen the hydrogen sorption properties of 38 different PdAu alloys in a single experiment.

Moreover, in **Paper II**, we have demonstrated the accelerating effect that plastic deformation through nanoindentation has on the hydrogen sorption kinetics of supported Pd nanoparticles. Also, this study revealed the intricate interplay between particle morphology, internal structure and substrate interaction that work together to decide the evolution of thermodynamic and kinetic properties of supported Pd nanoparticles under repeated hydrogen cycling.

The focus of near-term projects I plan to embark after this thesis is mainly on the microshutter method described in section 5.2., and its application to make tailored multi-alloy samples for plasmonic hydrogen sensing. Specifically, we for example aim to use machine learning methods to analyze the complex response of a large multi-alloy sample when exposed to hydrogen in a background of different types of gases that mimic specific real life sensor application environments, such as (humid) air with typical contaminants that include CO, NOx and SOx. In fact, a first prototype sample

for this project has already been fabricated and consists of 24 different binary and ternary alloys comprised of 4 different metals, with 45 particles per composition (Figure 22). To investigate this type of sample, a specialized measurement chamber that enables sample exposure to multiple gases simultaneously, as well as makes it possible to humidify the supplied gases is being built and is soon ready for the initial measurements on the multi-alloy sample.

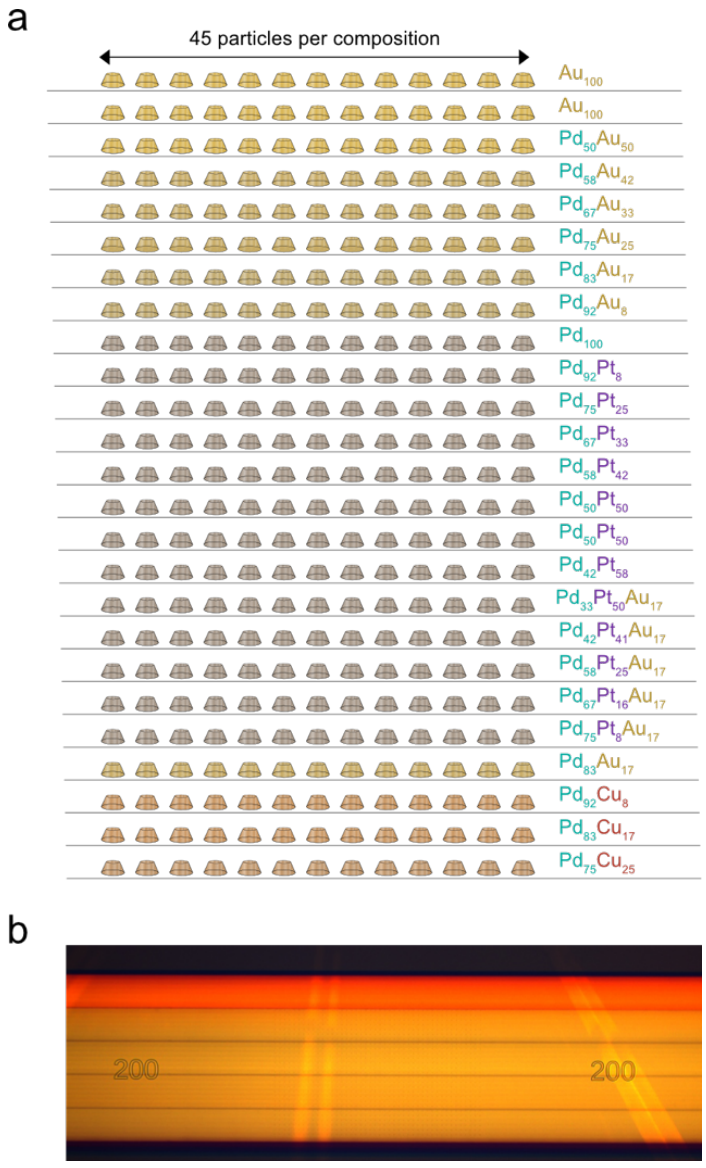

Figure 22: A multi-alloy sample made by the microshutter method. (a) Schematic of the sample outline. The sample consists of 25 particle rows of 24 different alloy and metal systems with 45 particles per row (*i.e.* per composition). (b) Optical micrograph of the mask area right after metal deposition but before mask lift-off. The imaged area is roughly 650 x 300 µm large and the horizontal bands of different metals are clearly visible.

Regarding the tedious dicing process described in section 5.2, We are also planning to improve this time-consuming process since it currently is limiting the efficiency of the entire concept. Currently, the focus is to limit the need of the dicing saw and instead develop a reproducible, wafer-scale etching process for fabricating the substrates required for the microshutter. The basis of this idea is to develop a dry-etch scheme to reproducibly etch high-precision substrates for the microshutter. However, since dry-etching through an entire Si-wafer of 500 μm thickness would not be time-efficient, the dry etching will only be used to define a thin, well-defined cut into the substrate (Figure 23a). Next, the sample would be flipped to the other side and diced from the backside – but not all the way through (Figure 23b). If done correctly, this would leave the edge made by the dry-etching intact, and as such, allow us to use this small but well-defined rim around the sample to define its overall geometry with respect to the microshutter slot (Figure 19b). A glaring question is of course how well-defined and reproducible we can etch by dry-etching, but this the future will tell.

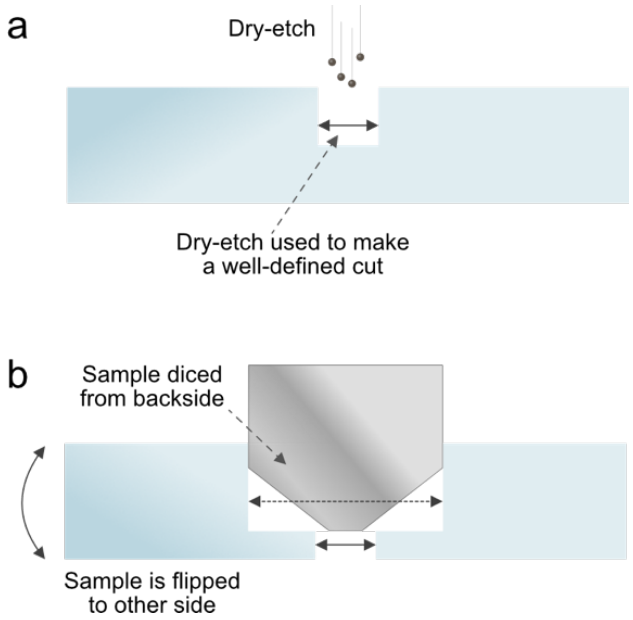

Figure 23: Etching concept for well-defined microshutter substrates. (a) A small but well-defined cut (solid arrow) is made into the Si wafer by dry-etching. (b) The wafer is thereafter flipped upside-down and diced from the backside. The dicing cut (dotted arrow) is less well-defined than the cut made by dry-etching (solid arrow), but as the wafer is not diced all the way through, this still leaves the well-defined edge made by etching as a rim around each sample.

Acknowledgments

I would like to acknowledge the funding provided by the Knut & Alice Wallenberg Foundation and the Swedish Foundation for Strategic Research.

I would like to thank my main supervisor Christoph, who gave me the opportunity to work with a project that I truly enjoy and whose advise have been critical for me to reach this point in my PhD.

I would like to thank Joachim, for whom the biggest hurdles in nanofabrication are merely setbacks.

I would like to thank my examiner Henrik, who gave me feedback on this thesis and strives to keep the division the best work place it can be.

I would like to thank past and present members of the Langhammer group, who are always willing to help out with small and large things in the lab.

I would like to thank past and present members of the division of Chemical Physics whose lunch company are always enjoyable.

I would like to thank Chalmers Materials Analysis Laboratory and Nanofabrication Laboratory, who provide the infrastructure necessary for high-end nanoscience.

References

(1) Moore, G. Moore's law. *Electronics Magazine* **1965**, *38* (8), 114.

(2) Rupp, K. Transistors per microprocessor. Our World in Data, **2022**.

(3) Eberle, A. L.; Mikula, S.; Schalek, R.; Lichtman, J.; Tate, M. L. K.; Zeidler, D. High-resolution, high-throughput imaging with a multibeam scanning electron microscope. *J Microsc* **2015**, *259* (2), 114-120. DOI: 10.1111/jmi.12224.

(4) Reinle-Schmitt, M.; Sisak Jung, D.; Morin, M.; Costa, F. N.; Casati, N.; Gozzo, F. Exploring high-throughput synchrotron X-Ray powder diffraction for the structural analysis of pharmaceuticals. *Int J Pharm X* **2023**, *6*, 100221. DOI: 10.1016/j.ijpx.2023.100221.

(5) Ndolomingo, M. J.; Bingwa, N.; Meijboom, R. Review of supported metal nanoparticles: synthesis methodologies, advantages and application as catalysts. *Journal of Materials Science* **2020**, *55* (15), 6195-6241. DOI: 10.1007/s10853-020-04415-x.

(6) Astruc, D. *Nanoparticles and catalysis*; John Wiley & Sons, **2008**.

(7) Darmadi, I.; Nugroho, F. A. A.; Langhammer, C. High-Performance Nanostructured Palladium-Based Hydrogen Sensors—Current Limitations and Strategies for Their Mitigation. *ACS Sensors* **2020**, *5* (11), 3306-3327. DOI: 10.1021/acssensors.0c02019.

(8) Albinsson, D.; Boje, A.; Nilsson, S.; Tiburski, C.; Hellman, A.; Ström, H.; Langhammer, C. Copper catalysis at operando conditions—bridging the gap between single nanoparticle probing and catalyst-bed-averaging. *Nature Communications* **2020**, *11* (1), 1-13. DOI: 10.1038/s41467-020-18623-1.

(9) Alekseeva, S.; Fanta, A. B. D. S.; Iandolo, B.; Antosiewicz, T. J.; Nugroho, F. A. A.; Wagner, J. B.; Burrows, A.; Zhdanov, V. P.; Langhammer, C. Grain boundary mediated hydriding phase transformations in individual polycrystalline metal nanoparticles. *Nature Communications* **2017**, *8* (1), 1084. DOI: 10.1038/s41467-017-00879-9.

(10) Alekseeva, S.; Strach, M.; Nilsson, S.; Fritzsche, J.; Zhdanov, V. P.; Langhammer, C. Grain-growth mediated hydrogen sorption kinetics and compensation effect in single Pd nanoparticles. *Nature Communications* **2021**, *12* (1), 5427. DOI: 10.1038/s41467-021-25660-x.

(11) Syrenova, S.; Wadell, C.; Nugroho, F. A. A.; Gschneidtner, T. A.; Diaz Fernandez, Y. A.; Nalin, G.; Świtlik, D.; Westerlund, F.; Antosiewicz, T. J.; Zhdanov, V. P.; et al. Hydride formation thermodynamics and hysteresis in individual Pd nanocrystals with different size and shape. *Nature Materials* **2015**, *14* (12), 1236-1244. DOI: 10.1038/nmat4409.

(12) *A hydrogen strategy for a climate-neutral Europe*; European Commission, **2020**.

(13) *U.S. National Clean Hydrogen Strategy and Roadmap*; U.S. Department of Energy, **2023**.

(14) *Australia's National Hydrogen Strategy*; Department of Climate Change, Energy, the Environment and Water, **2019**.

(15) *Basic Hydrogen Strategy*; Ministry of Economy Trade and Industry of Japan, **2017**.

(16) *Multi-Year Research, Development, and Demonstration Plan, 2011−2020. 3.7 Hydrogen Safety, Codes and Standards*; U.S. Department of Energy, **2015**.

(17) Keszei, E. *Chemical thermodynamics: an introduction*; Springer Science & Business Media, **2013**.

(18) Arrhenius, S. *Z. Physik Chem.* **1889**, *4*, 226.

(19) Mao, Z.; Campbell, C. T. Apparent Activation Energies in Complex Reaction Mechanisms: A Simple Relationship via Degrees of Rate Control. *ACS Catalysis* **2019**, *9* (10), 9465-9473. DOI: 10.1021/acscatal.9b02761.

(20) Kittel, C.; McEuen, P. *Introduction to solid state physics*; John Wiley & Sons, **2018**.

(21) Haidemenopoulos, G. N. *Physical Metallurgy*; CRC Press, **2018**. DOI: 10.1201/9781315211220.

(22) Kraftmakher, Y. Equilibrium vacancies and thermophysical properties of metals. *Physics Reports* **1998**, *299* (2-3), 79-188.

(23) Chen, C. C.; Zhu, C.; White, E. R.; Chiu, C. Y.; Scott, M. C.; Regan, B. C.; Marks, L. D.; Huang, Y.; Miao, J. Three-dimensional imaging of dislocations in a nanoparticle at atomic resolution. *Nature* **2013**, *496* (7443), 74-77. DOI: 10.1038/nature12009.

(24) Nilsson Pingel, T.; Jorgensen, M.; Yankovich, A. B.; Gronbeck, H.; Olsson, E. Influence of atomic site-specific strain on catalytic activity of supported nanoparticles. *Nat Commun* **2018**, *9* (1), 2722. DOI: 10.1038/s41467-018-05055-1.

(25) Bisht, A.; Koju, R. K.; Qi, Y.; Hickman, J.; Mishin, Y.; Rabkin, E. The impact of alloying on defect-free nanoparticles exhibiting softer but tougher behavior. *Nat Commun* **2021**, *12* (1), 2515. DOI: 10.1038/s41467-021-22707-x.

(26) Liang, Z.; Rabkin, E. The effect of composition and long-range order on the strength of defect-free faceted Cu-Au nanoparticles. *Acta Materialia* **2024**, *266*. DOI: 10.1016/j.actamat.2024.119680.

(27) Sharma, A.; Hickman, J.; Gazit, N.; Rabkin, E.; Mishin, Y. Nickel nanoparticles set a new record of strength. *Nature Communications* **2018**, *9* (1), 4102. DOI: 10.1038/s41467-018-06575-6.

(28) Sharma, A.; Kositski, R.; Kovalenko, O.; Mordehai, D.; Rabkin, E. Giant shape- and size-dependent compressive strength of molybdenum nano- and microparticles. *Acta Materialia* **2020**, *198*, 72-84. DOI: 10.1016/j.actamat.2020.07.054.

(29) Flanagan, T. J.; Kovalenko, O.; Rabkin, E.; Lee, S.-W. The effect of defects on strength of gold microparticles. *Scripta Materialia* **2019**, *171*, 83-86. DOI: 10.1016/j.scriptamat.2019.06.023.

(30) Taylor, G. I. The mechanism of plastic deformation of crystals. Part I.—Theoretical. *Proceedings of the Royal Society of London. Series A, Containing Papers of a Mathematical and Physical Character* **1934**, *145* (855), 362-387.

(31) Orowan, E. For crystal plasticity. III. *Z Phys* **1934**, *89* (9-10), 634-659. DOI: Doi 10.1007/Bf01341480.

(32) Polanyi, M. Über eine Art Gitterstörung, die einen Kristall plastisch machen könnte. *Z Phys* **1934**, *89* (9-10), 660-664.

(33) Legros, M.; Dehm, G.; Arzt, E.; Balk, T. J. Observation of giant diffusivity along dislocation cores. *Science* **2008**, *319* (5870), 1646-1649.

(34) Rabier, J.; Puls, M. Atomistic calculations of point-defect interaction and migration energies in the core of an edge dislocation in NaCl. *Philosophical Magazine A* **1989**, *59* (3), 533-546.

(35) Lu, K. Stabilizing nanostructures in metals using grain and twin boundary architectures. *Nature Reviews Materials* **2016**, *1* (5), 1-13.

(36) Swiatnicki, W.; Łojkowski, W.; Grabski, M. W. Investigation of grain boundary diffusion in polycrystals by means of extrinsic grain boundary dislocations spreading rate. *Acta Metallurgica* **1986**, *34* (4), 599-605.

(37) Han, J.; Thomas, S. L.; Srolovitz, D. J. Grain-boundary kinetics: A unified approach. *Progress in Materials Science* **2018**, *98*, 386-476.

(38) Manchester, F.; San-Martin, A.; Pitre, J. The H-Pd (hydrogen-palladium) system. *Journal of phase equilibria* **1994**, *15* (1), 62-83.

(39) Bronze. In *Encyclopaedia Britannica*, **2024**.

(40) Adams, B. D.; Chen, A. The role of palladium in a hydrogen economy. *Materials Today* **2011**, *14* (6), 282-289. DOI: 10.1016/S1369-7021(11)70143-2.

(41) Behm, R. J.; Penka, V.; Cattania, M. G.; Christmann, K.; Ertl, G. Evidence for ‘‘subsurface’’ hydrogen on Pd(110): An intermediate between chemisorbed and dissolved species. *The Journal of Chemical Physics* **1983**, *78* (12), 7486-7490. DOI: 10.1063/1.444739.

(42) Grönbeck, H.; Zhdanov, V. P. Effect of lattice strain on hydrogen diffusion in Pd: A density functional theory study. *Physical Review B* **2011**, *84* (5). DOI: 10.1103/PhysRevB.84.052301.

(43) Schwarzer, M.; Hertl, N.; Nitz, F.; Borodin, D.; Fingerhut, J.; Kitsopoulos, T. N.; Wodtke, A. M. Adsorption and Absorption Energies of Hydrogen with Palladium. *J Phys Chem C Nanomater Interfaces* **2022**, *126* (34), 14500-14508. DOI: 10.1021/acs.jpcc.2c04567.

(44) Delmelle, R.; Bamba, G.; Proost, J. In-situ monitoring of hydride formation in Pd thin film systems. *International Journal of Hydrogen Energy* **2010**, *35* (18), 9888-9892. DOI: 10.1016/j.ijhydene.2009.11.087.

(45) Hu, Z.; Thundat, T.; Warmack, R. Investigation of adsorption and absorption-induced stresses using microcantilever sensors. *Journal of Applied Physics* **2001**, *90* (1), 427-431.

(46) Firth, J. B. XXII.—The sorption of hydrogen by palladium at low temperatures. *Journal of the Chemical Society, Transactions* **1920**, *117*, 171-183.

(47) Kirchheim, R.; Pundt, A. Hydrogen in Metals, Fifth Edit. Elsevier: **2014**.

(48) Griessen, R.; Strohfeldt, N.; Giessen, H. Thermodynamics of the hybrid interaction of hydrogen with palladium nanoparticles. *Nature Materials* **2016**, *15* (3), 311-317. DOI: 10.1038/nmat4480.

(49) Ulvestad, A.; Welland, M. J.; Cha, W.; Liu, Y.; Kim, J. W.; Harder, R.; Maxey, E.; Clark, J. N.; Highland, M. J.; You, H.; et al. Three-dimensional

imaging of dislocation dynamics during the hydriding phase transformation. *Nature Materials* **2017**, *16* (5), 565-571. DOI: 10.1038/nmat4842.

(50) Schwarz, R. B.; Khachaturyan, A. G. Thermodynamics of open two-phase systems with coherent interfaces: Application to metal-hydrogen systems. *Acta Materialia* **2006**, *54* (2), 313-323. DOI: 10.1016/j.actamat.2005.08.044.

(51) Baldi, A.; Narayan, T. C.; Koh, A. L.; Dionne, J. A. In situ detection of hydrogen-induced phase transitions in individual palladium nanocrystals. *Nature Materials* **2014**, *13* (12), 1143-1148. DOI: 10.1038/nmat4086.

(52) Wicke, E.; Blaurock, J. New experiments on and interpretations of hysteresis effects of Pd-D2 and Pd-H2. *Journal of the Less Common Metals* **1987**, *130*, 351-363.

(53) Feenstra, R.; Griessen, R.; De Groot, D. Hydrogen induced lattice expansion and effective HH interaction in single phase PdHc. *Journal of Physics F: Metal Physics* **1986**, *16* (12), 1933.

(54) Alefeld, G. Phase transitions of hydrogen in metals due to elastic interaction. *Berichte der Bunsengesellschaft für physikalische Chemie* **1972**, *76* (8), 746-755.

(55) Horner, H.; Wagner, H. A model calculation for the α-α'phase transition in metal-hydrogen systems. *Journal of Physics C: Solid State Physics* **1974**, *7* (18), 3305.

(56) Fukai, Y. *The Metal-Hydrogen System*; Springer Berlin Heidelberg, **2005**. DOI: 10.1007/3-540-28883-X.

(57) Wagner, S.; Pundt, A. Quasi-thermodynamic model on hydride formation in palladium–hydrogen thin films: Impact of elastic and microstructural constraints. *International journal of hydrogen energy* **2016**, *41* (4), 2727-2738.

(58) Wagner, S.; Kramer, T.; Uchida, H.; Dobron, P.; Cizek, J.; Pundt, A. Mechanical stress and stress release channels in 10–350 nm palladium

hydrogen thin films with different micro-structures. *Acta Materialia* **2016**, *114*, 116-125.

(59) Amin-Ahmadi, B.; Connétable, D.; Fivel, M.; Tanguy, D.; Delmelle, R.; Turner, S.; Malet, L.; Godet, S.; Pardoen, T.; Proost, J. Dislocation/hydrogen interaction mechanisms in hydrided nanocrystalline palladium films. *Acta Materialia* **2016**, *111*, 253-261.

(60) Pivak, Y.; Schreuders, H.; Slaman, M.; Griessen, R.; Dam, B. Thermodynamics, stress release and hysteresis behavior in highly adhesive Pd–H films. *International Journal of Hydrogen Energy* **2011**, *36* (6), 4056-4067. DOI: 10.1016/j.ijhydene.2010.12.063.

(61) Bannenberg, L. J.; Nugroho, F. A. A.; Schreuders, H.; Norder, B.; Trinh, T. T.; Steinke, N. J.; Van Well, A. A.; Langhammer, C.; Dam, B. Direct Comparison of PdAu Alloy Thin Films and Nanoparticles upon Hydrogen Exposure. *ACS Applied Materials and Interfaces* **2019**, *11* (17), 15489-15497. DOI: 10.1021/acsami.8b22455.

(62) Isaac, N.; Ngene, P.; Westerwaal, R.; Gaury, J.; Dam, B.; Schmidt-Ott, A.; Biskos, G. Optical hydrogen sensing with nanoparticulate Pd–Au films produced by spark ablation. *Sensors and Actuators B: Chemical* **2015**, *221*, 290-296.

(63) Westerwaal, R.; Rooijmans, J.; Leclercq, L.; Gheorghe, D.; Radeva, T.; Mooij, L.; Mak, T.; Polak, L.; Slaman, M.; Dam, B. Nanostructured Pd–Au based fiber optic sensors for probing hydrogen concentrations in gas mixtures. *International Journal of Hydrogen Energy* **2013**, *38* (10), 4201-4212.

(64) Darmadi, I.; Khairunnisa, S. Z.; Tomeček, D.; Langhammer, C. Optimization of the Composition of PdAuCu Ternary Alloy Nanoparticles for Plasmonic Hydrogen Sensing. *ACS Applied Nano Materials* **2021**, *4* (9), 8716-8722. DOI: 10.1021/acsanm.1c01242.

(65) Darmadi, I.; Nugroho, F. A. A.; Kadkhodazadeh, S.; Wagner, J. B.; Langhammer, C. Rationally Designed PdAuCu Ternary Alloy Nanoparticles for Intrinsically Deactivation-Resistant Ultrafast Plasmonic Hydrogen

Sensing. *ACS Sensors* **2019**, *4* (5), 1424-1432. DOI: 10.1021/acssensors.9b00610.

(66) Nugroho, F. A. A.; Darmadi, I.; Zhdanov, V. P.; Langhammer, C. Universal Scaling and Design Rules of Hydrogen-Induced Optical Properties in Pd and Pd-Alloy Nanoparticles. *ACS Nano* **2018**, *12* (10), 9903-9912. DOI: 10.1021/acsnano.8b02835.

(67) Nugroho, F. A. A.; Eklund, R.; Nilsson, S.; Langhammer, C. A fiber-optic nanoplasmonic hydrogen sensor: Via pattern-transfer of nanofabricated PdAu alloy nanostructures. *Nanoscale* **2018**, *10* (44), 20533-20539. DOI: 10.1039/c8nr03751e.

(68) Opalka, S.; Huang, W.; Wang, D.; Flanagan, T.; Løvvik, O.; Emerson, S.; She, Y.; Vanderspurt, T. Hydrogen interactions with the PdCu ordered B2 alloy. *Journal of Alloys and Compounds* **2007**, *446*, 583-587.

(69) Galipaud, J.; Martin, M.; Roué, L.; Guay, D. Pulsed laser deposition of PdCuAu alloy membranes for hydrogen absorption study. *The Journal of Physical Chemistry C* **2015**, *119* (47), 26451-26458.

(70) Amandusson, H.; Ekedahl, L.-G.; Dannetun, H. Hydrogen permeation through surface modified Pd and PdAg membranes. *Journal of Membrane Science* **2001**, *193* (1), 35-47.

(71) Sonwane, C. G.; Wilcox, J.; Ma, Y. H. Achieving optimum hydrogen permeability in PdAg and PdAu alloys. *Journal of Chemical Physics* **2006**, *125* (18). DOI: 10.1063/1.2387166.

(72) Wadell, C.; Nugroho, F. A. A.; Lidström, E.; Iandolo, B.; Wagner, J. B.; Langhammer, C. Hysteresis-free nanoplasmonic pd-au alloy hydrogen sensors. *Nano Letters* **2015**, *15* (5), 3563-3570. DOI: 10.1021/acs.nanolett.5b01053.

(73) Namba, K.; Ogura, S.; Ohno, S.; Di, W.; Kato, K.; Wilde, M.; Pletikosić, I.; Pervan, P.; Milun, M.; Fukutani, K. Acceleration of hydrogen absorption by palladium through surface alloying with gold. *Proceedings of the National*

Academy of Sciences **2018**, *115* (31), 7896-7900. DOI: 10.1073/pnas.1800412115.

(74) Nugroho, F. A. A.; Darmadi, I.; Cusinato, L.; Susarrey-Arce, A.; Schreuders, H.; Bannenberg, L. J.; da Silva Fanta, A. B.; Kadkhodazadeh, S.; Wagner, J. B.; Antosiewicz, T. J.; et al. Metal–polymer hybrid nanomaterials for plasmonic ultrafast hydrogen detection. *Nature Materials* **2019**, *18* (5), 489-495. DOI: 10.1038/s41563-019-0325-4.

(75) Wicke, E.; Brodowsky, H.; Züchner, H. Hydrogen in palladium and palladium alloys. In *Hydrogen in Metals II: Application-Oriented Properties*, Alefeld, G., Völkl, J. Eds.; Springer Berlin Heidelberg, 1978; pp 73-155.

(76) Myers, S. M.; Baskes, M.; Birnbaum, H.; Corbett, J. W.; DeLeo, G.; Estreicher, S.; Haller, E. E.; Jena, P.; Johnson, N. M.; Kirchheim, R. Hydrogen interactions with defects in crystalline solids. *Reviews of Modern Physics* **1992**, *64* (2), 559.

(77) Kirchheim, R. Interaction of hydrogen with dislocations in palladium—I. Activity and diffusivity and their phenomenological interpretation. *Acta Metallurgica* **1981**, *29* (5), 835-843.

(78) Mütschele, T.; Kirchheim, R. Segregation and diffusion of hydrogen in grain boundaries of palladium. *Scripta metallurgica* **1987**, *21* (2), 135-140.

(79) Pundt, A.; Kirchheim, R. HYDROGEN IN METALS: Microstructural Aspects. *Annual Review of Materials Research* **2006**, *36* (1), 555-608. DOI: 10.1146/annurev.matsci.36.090804.094451.

(80) Deutges, M.; Barth, H. P.; Chen, Y.; Borchers, C.; Kirchheim, R. Hydrogen diffusivities as a measure of relative dislocation densities in palladium and increase of the density by plastic deformation in the presence of dissolved hydrogen. *Acta Materialia* **2015**, *82*, 266-274.

(81) Čížek, J.; Melikhova, O.; Dobroň, P.; Hruška, P. In-situ characterization of hydrogen-induced defects in palladium by positron annihilation and

acoustic emission. *International Journal of Hydrogen Energy* **2017**, *42* (35), 22460-22467. DOI: 10.1016/j.ijhydene.2017.04.275.

(82) Lumbeeck, G.; Idrissi, H.; Amin-Ahmadi, B.; Favache, A.; Delmelle, R.; Samaee, V.; Proost, J.; Pardoen, T.; Schryvers, D. Effect of hydriding induced defects on the small-scale plasticity mechanisms in nanocrystalline palladium thin films. *Journal of Applied Physics* **2018**, *124* (22). DOI: 10.1063/1.5055274.

(83) Kirchheim, R. Hydrogen solubility and diffusivity in defective and amorphous metals. *Progress in Materials Science* **1988**, *32* (4), 261-325.

(84) Kirchheim, R. Lattice discontinuities affecting the generation and annihilation of diffusible hydrogen and vice versa. *Philosophical Transactions of the Royal Society A: Mathematical, Physical and Engineering Sciences* **2017**, *375* (2098), 20160403.

(85) Delmelle, R.; Amin-Ahmadi, B.; Sinnaeve, M.; Idrissi, H.; Pardoen, T.; Schryvers, D.; Proost, J. Effect of structural defects on the hydriding kinetics of nanocrystalline Pd thin films. *International Journal of Hydrogen Energy* **2015**, *40* (23), 7335-7347. DOI: 10.1016/j.ijhydene.2015.04.017.

(86) Ulvestad, A.; Yau, A. The self-healing of defects induced by the hydriding phase transformation in palladium nanoparticles. *Nature Communications* **2017**, *8* (1), 1-6. DOI: 10.1038/s41467-017-01548-7.

(87) Weadock, N. J.; Voorhees, P. W.; Fultz, B. Interface pinning causes the hysteresis of the hydride transformation in binary metal hydrides. *Physical Review Materials* **2021**, *5* (1), 13604. DOI: 10.1103/PhysRevMaterials.5.013604.

(88) Langhammer, C.; Zorić, I.; Larsson, E. M.; Kasemo, B. Localized surface plasmons shed light on nanoscale metal hydrides. *Advanced Materials* **2010**, *22* (41), 4628-4633. DOI: 10.1002/adma.201000973.

(89) Larsson, E. M.; Edvardsson, M. E.; Langhammer, C.; Zorić, I.; Kasemo, B. A combined nanoplasmonic and electrodeless quartz crystal microbalance setup. *Review of Scientific Instruments* **2009**, *80* (12).

(90) Larsson, E. M.; Syrenova, S.; Langhammer, C. Nanoplasmonic sensing for nanomaterials science. *Nanophotonics* **2012**, *1* (3-4), 249-266.

(91) Tittl, A.; Giessen, H.; Liu, N. Plasmonic gas and chemical sensing. *Nanophotonics* **2014**, *3* (3), 157-180.

(92) Mayer, K. M.; Hafner, J. H. Localized Surface Plasmon Resonance Sensors. *Chemical Reviews* **2011**, *111* (6), 3828-3857. DOI: 10.1021/cr100313v.

(93) Taylor, A. B.; Zijlstra, P. Single-molecule plasmon sensing: current status and future prospects. *ACS sensors* **2017**, *2* (8), 1103-1122.

(94) Tian, L.; Fei, M.; Kattumenu, R.; Abbas, A.; Singamaneni, S. Gold nanorods as nanotransducers to monitor the growth and swelling of ultrathin polymer films. *Nanotechnology* **2012**, *23* (25), 255502.

(95) Langhammer, C.; Zorić, I.; Kasemo, B.; Clemens, B. M. Hydrogen storage in Pd nanodisks characterized with a novel nanoplasmonic sensing scheme. *Nano Letters* **2007**, *7* (10), 3122-3127.

(96) Tabib Zadeh Adibi, P.; Pingel, T.; Olsson, E.; Gronbeck, H.; Langhammer, C. Plasmonic nanospectroscopy of platinum catalyst nanoparticle sintering in a mesoporous alumina support. *ACS nano* **2016**, *10* (5), 5063-5069.

(97) Langhammer, C.; Larsson, E. M.; Kasemo, B.; Zoric, I. Indirect nanoplasmonic sensing: ultrasensitive experimental platform for nanomaterials science and optical nanocalorimetry. *Nano letters* **2010**, *10* (9), 3529-3538.

(98) Nugroho, F. A.; Diaz de Zerio Mendaza, A.; Lindqvist, C.; Antosiewicz, T. J.; Muller, C.; Langhammer, C. Plasmonic nanospectroscopy for thermal analysis of organic semiconductor thin films. *Analytical chemistry* **2017**, *89* (4), 2575-2582.

(99) Chan, G. H.; Zhao, J.; Hicks, E. M.; Schatz, G. C.; Van Duyne, R. P. Plasmonic properties of copper nanoparticles fabricated by nanosphere lithography. *Nano letters* **2007**, *7* (7), 1947-1952.

(100) Larsson, E. M.; Millet, J.; Gustafsson, S.; Skoglundh, M.; Zhdanov, V. P.; Langhammer, C. Real time indirect nanoplasmonic in situ spectroscopy of catalyst nanoparticle sintering. *Acs Catalysis* **2012**, *2* (2), 238-245.

(101) Zheng, Y. B.; Huang, T. J.; Desai, A. Y.; Wang, S. J.; Tan, L. K.; Gao, H.; Huan, A. C. H. Thermal behavior of localized surface plasmon resonance of Au⁄TiO2 core/shell nanoparticle arrays. *Applied Physics Letters* **2007**, *90* (18).

(102) Suh, J.; Donev, E.; Ferrara, D.; Tetz, K.; Feldman, L.; Haglund, R. Modulation of the gold particle–plasmon resonance by the metal–semiconductor transition of vanadium dioxide. *Journal of Optics A: Pure and Applied Optics* **2008**, *10* (5), 055202.

(103) Tiburski, C.; Boje, A.; Nilsson, S.; Say, Z.; Fritzsche, J.; Ström, H.; Hellman, A.; Langhammer, C. Light-Off in Plasmon-Mediated Photocatalysis. *ACS Nano* **2021**, *15* (7), 11535-11542. DOI: 10.1021/acsnano.1c01537.

(104) Tiburski, C.; Nugroho, F. A. A.; Langhammer, C. Optical Hydrogen Nanothermometry of Plasmonic Nanoparticles under Illumination. *ACS nano* **2022**, *16* (4), 6233-6243.

(105) Alekseeva, S.; Nedrygailov, I. I.; Langhammer, C. Single Particle Plasmonics for Materials Science and Single Particle Catalysis. *ACS Photonics* **2019**, *6* (6), 1319-1330. DOI: 10.1021/acsphotonics.9b00339.

(106) Poyli, M. A.; Silkin, V. M.; Chernov, I. P.; Echenique, P. M.; Muiño, R. D.; Aizpurua, J. Multiscale Theoretical Modeling of Plasmonic Sensing of Hydrogen Uptake in Palladium Nanodisks. *The Journal of Physical Chemistry Letters* **2012**, *3* (18), 2556-2561. DOI: 10.1021/jz3007723.

(107) Ekborg-Tanner, P.; Rahm, J. M.; Rosendal, V.; Bancerek, M.; Rossi, T. P.; Antosiewicz, T. J.; Erhart, P. Computational Design of Alloy

Nanostructures for Optical Sensing of Hydrogen. *ACS Applied Nano Materials* **2022**, *5* (8), 10225-10236. DOI: 10.1021/acsanm.2c01189.

(108) Silkin, V. M.; Diez Muino, R.; Chernov, I. P.; Chulkov, E. V.; Echenique, P. M. Tuning the plasmon energy of palladium-hydrogen systems by varying the hydrogen concentration. *J Phys Condens Matter* **2012**, *24* (10), 104021. DOI: 10.1088/0953-8984/24/10/104021.

(109) Wadell, C.; Nugroho, F. A. A.; Lidstrom, E.; Iandolo, B.; Wagner, J. B.; Langhammer, C. Hysteresis-free nanoplasmonic Pd–Au alloy hydrogen sensors. *Nano letters* **2015**, *15* (5), 3563-3570.

(110) Langhammer, C.; Zhdanov, V. P.; Zorić, I.; Kasemo, B. Size-Dependent Kinetics of Hydriding and Dehydriding of Pd Nanoparticles. *Physical Review Letters* **2010**, *104* (13), 135502. DOI: 10.1103/PhysRevLett.104.135502.

(111) Andersson, C.; Serebrennikova, O.; Tiburski, C.; Alekseeva, S.; Fritzsche, J.; Langhammer, C. A Microshutter for the Nanofabrication of Plasmonic Metal Alloys with Single Nanoparticle Composition Control. *ACS nano* **2023**, *17* (16), 15978-15988.

(112) Nugroho, F. A. A.; Iandolo, B.; Wagner, J. B.; Langhammer, C. Bottom-Up Nanofabrication of Supported Noble Metal Alloy Nanoparticle Arrays for Plasmonics. *ACS Nano* **2016**, *10* (2), 2871-2879. DOI: 10.1021/acsnano.5b08057.

(113) Kadkhodazadeh, S.; Nugroho, F. A. A.; Langhammer, C.; Beleggia, M.; Wagner, J. B. Optical Property-Composition Correlation in Noble Metal Alloy Nanoparticles Studied with EELS. *ACS Photonics* **2019**, *6* (3), 779-786. DOI: 10.1021/acsphotonics.8b01791.

(114) Rahm, J. M.; Tiburski, C.; Rossi, T. P.; Nugroho, F. A. A.; Nilsson, S.; Langhammer, C.; Erhart, P. A Library of Late Transition Metal Alloy Dielectric Functions for Nanophotonic Applications. *Advanced Functional Materials* **2020**, *30* (35), 2002122. DOI: 10.1002/adfm.202002122.

(115) Zimmerman, J.; Bisht, A.; Mishin, Y.; Rabkin, E. Size and shape effects on the strength of platinum nanoparticles. *Journal of Materials Science* **2021**, *56* (32), 18300-18312. DOI: 10.1007/s10853-021-06435-7.